J. Fluid Mech. (2001), *vol.* 446, *pp.* 25–65. © 2001 Cambridge University Press
DOI: 10.1017/S0022112001005638 Printed in the United Kingdom

Experiments on the stability and transition of wind-driven water surfaces

By FABRICE VERON AND W. KENDALL MELVILLE

Scripps Institution of Oceanography, University of California, San Diego, La Jolla, CA 92093-0213, USA

(Received 24 September 2000 and in revised form 14 April 2000)

We present the results of laboratory and field measurements on the stability of wind-driven water surfaces. The laboratory measurements show that when exposed to an increasing wind starting from rest, surface current and wave generation is accompanied by a variety of phenomena that occur over comparable space and time scales. Of particular interest is the generation of small-scale, streamwise vortices, or Langmuir circulations, the clear influence of the circulations on the structure of the growing wave field, and the subsequent transition to turbulence of the surface flow. Following recent work by Melville, Shear & Veron (1998) and Veron & Melville (1999*b*), we show that the waves that are initially generated by the wind are then strongly modulated by the Langmuir circulations that follow. Direct measurements of the modulated wave variables are qualitatively consistent with geometrical optics and wave action conservation, but quantitative comparison remains elusive. Within the range of parameters of the experiments, both the surface waves and the Langmuir circulations first appear at constant Reynolds numbers of 370 ± 10 and 530 ± 20, respectively, based on the surface velocity and the depth of the laminar shear layer. The onset of the Langmuir circulations leads to a significant increase in the heat transfer across the surface. The field measurements in a boat basin display the same phenomena that are observed in the laboratory. The implications of the measurements for air–sea fluxes, especially heat and gas transfer, and sea-surface temperature, are discussed.

1. Introduction

The air–sea interface comprises approximately 70% of the Earth's surface and, with the globally averaged wind speed (traditionally, U_{10}, the wind speed at 10 m) in the range of 6–8 m s^{-1}, much of the time the air–sea interface is in a low-wind regime. Winds generate waves and currents, but despite the interest in both processes since antiquity, there is no comprehensive understanding of the full complexity of the evolution of the wind-generated wavy surface-current field. Modern theories of wind-wave generation begin with Miles' (1957) consideration of an inviscid instability of the shear flow in the air, which paid particular attention to the role of the critical layer at which the wind speed matches the phase speed of the waves. Developments of the theory to account for the role of turbulence in the air have led to improved agreement with measurements (see Belcher & Hunt 1998 and references therein). Valenzuela (1976) and Kawai (1979) both studied the instability to gravity–capillary waves of the coupled air–water flow using Orr–Sommerfeld equations for each layer

with a log-linear turbulent wind profile in the air and a laminar profile in the water. Wheless & Csanady (1993) extended this method using a continuously differentiable form for the wind profile that approximates the log-linear profile. The predictions of the initial growth rate of the waves compare favourably with the data of Larson & Wright (1975) and Kawai's own data, but Kawai observed that the wave field quickly became three-dimensional.

Recently Melville, Shear & Veron (1998) described experiments on the evolution of the surface shear layer in water driven from rest by an accelerating wind. The experiments focused on the generation of Langmuir circulations, which are streamwise vortices near the surface accompanied by regions of surface convergence and divergence, that quickly evolved into fully developed turbulence. It was found that initially the surface layer accelerated under the wind stress, surface waves were generated and then the shear layer became unstable to Langmuir circulations. The Langmuir circulations led to a rapid mixing down of the momentum in the surface layer. The length and time scales for the generation of both waves and Langmuir circulations were found to be comparable, suggesting that the initial generation and evolution of both phenomena should be considered together.

The current theory of Langmuir circulations has focused on the Craik–Leibovich CLII mechanism with $O(\epsilon^2)$ scaling (Craik 1977; Leibovich 1977, 1983). The theory assumes that the Eulerian wind-driven surface current is $O(\epsilon)$ when compared with the orbital motions of a stationary homogeneous surface wave field, which are in turn $O(\epsilon)$ compared to the phase speed of the waves. Averaging over the fast (orbital) time scales leads to an additional vortex force which is the vector product of the Stokes drift and the vorticity of the Eulerian current. It is the vortex force that leads the surface current to be unstable to Langmuir circulations. Craik (1982*a*, *b*) investigated the CLII theory for $O(\epsilon)$ and $O(1)$ scaling, considering simple limiting cases of instability. For $O(1)$ scaling, there is a feedback from the Langmuir circulations to the waves, modulating the waves. The details of the evolution of surface currents and waves under realistic formulations of $O(1)$ scaling are still the subject of theoretical and numerical research (Phillips & Wu 1994).

Melville *et al.* (1998) provided some preliminary kinematic evidence that the cases they measured experimentally corresponded to $O(1)$ scaling, but their measurements of the surface currents and wave fields were not conclusive. The Langmuir circulations they measured had scales of $O(1–10)$ cm compared to the scales of $O(1–100)$ m usually measured in the field, casting some doubt on whether the phenomena measured in the laboratory are the same as those measured in the field. However, the typical field measurements are limited by the $O(1–10)$ m resolution of the acoustic Doppler sonars that are used to scatter off the bubbles that collect in the regions of convergence of the Langmuir circulations (Smith, Pinkel & Weller 1987; Smith 1992; Plueddemann *et al.* 1996; Smith 1998). Thus, if smaller-scale Langmuir circulations were present, they would not measure them. Smaller-scale circulations have been observed in lakes and other water bodies (Kenney 1993), but quantitative measurements are elusive, or affected by finite depth effects in shallow water (Szeri 1996). Indeed, the difficulty of measuring the smaller scales was mentioned by Langmuir (1938) himself in his pioneering work:

> Quantitative measurements of the streak spacings are difficult because between the well-defined streaks there are numerous smaller and less well-defined streaks. Just as large waves have smaller waves upon them, it appears that surfaces of larger vortices contain smaller and shallower vortices.

Scott *et al.* (1969) also observed that

> ... there often appear to be two types of streaks. One type lasted for a long time with winds greater than 3 m/sec while the other appeared briefly during gusts. Frequently one to three poorly defined short streaks appeared between long well defined streaks. In such cases, when the wind died the well defined streaks remained for some time and the short ones disappeared quickly.

Together with the recent measurements of Melville *et al.* (1998), these observations support the existence of small-scale, transient Langmuir circulations.

It is clear that the stability, transition and subsequent mixing at the surface of the ocean and other natural water bodies are of great importance for many processes, from local to global. While attention has focused on larger-scale longer-term phenomena, the mechanisms involved in small-scale mixing remain rather poorly understood. In fact, very little is known about their intermittent nature, which may very well dominate the long-term behaviour of the upper layers of the ocean at low wind speeds.

In this paper, we present quantitative measurements of the waves and small-scale Langmuir circulations which appear as transition phenomena in developing surface shear flows. In § 2 we describe the experimental facility and the instruments used. In § 3, we present the results from the laboratory experiments. Section 4 describes the results from a field experiment, and in § 5 we discuss the results in the context of air–sea fluxes.

A preliminary version of this work was presented at the Air-Sea Interface Symposium, Sydney, January 1999 (Veron & Melville 1999*b*).

2. Experimental setup

2.1. *Experimental facility*

The experiments were performed in the large wind-wave channel at the hydraulics laboratory, Scripps Institution of Oceanography (figure 1). The channel, 40 m long, 2.44 m high and 2.44 m wide, is equipped with a computer-controlled hydraulically actuated fan that exhausts to the atmosphere outside the laboratory. The channel was specially modified for these experiments with the addition of a new inlet section giving a 4-to-1 contraction ratio between the inlet and the working section. Downstream of the contraction, the wind tunnel section is smoothly contoured so that its bottom wall becomes horizontal 122.4 cm above the bottom of the channel. The optimum water level for a smooth transition between the solid air tunnel and the water surface is 122.4 cm; however, we chose a still water depth of 125 cm to account for the surface displacement due to the waves and the set-up in the tank, while retaining a smooth entry of the wind tunnel into the water. The water depth was kept at 125 cm for all the experiments described here. Experiments were repeated at five different fetches: 0.93, 4.60, 10.72, 15.62, and 19.29 m, where the fetch is defined as the distance from the intersection of the inlet section with the quiescent water surface to the centre of the frame of the colour imaging slope gauge (CISG) described below. The coordinate axes are chosen as shown in figure 1 where x is the along-wind direction, y the cross-wind direction, and z is vertically upwards with $z = 0$ at the quiescent water surface. Unless otherwise noted, all surface images and figures will be shown with this convention with the wind direction from left to right. The surface of the water was continuously skimmed with a diatomaceous earth filter pump which was turned off prior to the experiments. Air temperature, relative humidity and atmospheric pressure were recorded each day of the experiments (Weather monitor 2, Davis Instruments,

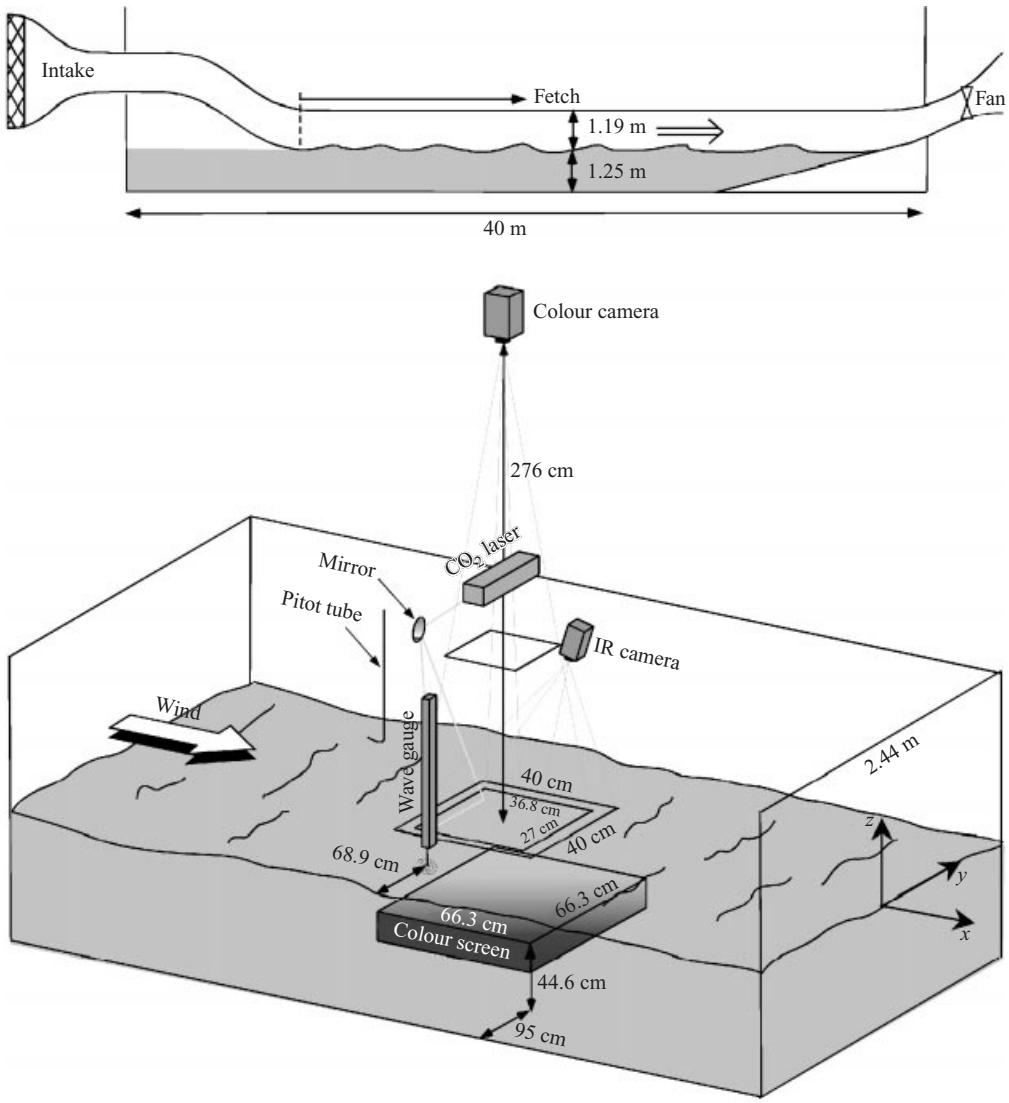

FIGURE 1. Instrument setup in the large wind-wave facility at Scripps Institution of Oceanography, University of California, San Diego.

Baltimore, MD). The instrument setup shown in figure 1 includes a colour imaging slope gauge (CISG), an infrared camera (IR camera), a Pitot static tube, a resistance wire wave gauge, and a CO_2 laser with a scanning mirror.

2.2. *Instrumentation*

2.2.1. *Colour Imaging Slope Gauge (CISG)*

The Colour Imaging Slope Gauge, a system derived from the pioneering work of Cox (1958), is based on the refraction of light across the air–water interface according to Snell's law, providing a relatively easy way to measure the slope of the surface. Our system is based on those developed by Jähne & Wass (1989) and Zhang & Cox (1994). An underwater light box (66.3 cm × 66.3 cm × 16.6 cm) is equipped with a set of closely spaced neon tubes and an upper translucent colour screen (Duratran,

Kodak) so that each point on the screen has a unique colour. This is accomplished by overlaying a linear gradient of red and green in the along-wind and cross-wind directions, respectively, and a uniform blue level. A 3-CCD colour video camera (Sony Model XC-003) is mounted 276 cm above the water surface: optical infinity when compared to the wave height. The local slope of the surface is measured by the colour difference that results from refraction through the surface. The gradients in the along-wind and cross-wind directions permit the retrieval of both the along-wind and cross-wind slopes, S_x and S_y, respectively. The system gives three non-interlaced 240×660 pixel RGB (Red, Green and Blue) images with a 59.94 Hz (60 Hz) frame rate and an 8 bit resolution for each colour. For the experiments described here, the camera operated either in the 60 Hz mode, or was triggered at a 6 Hz rate for the acquisition of longer time series. The data were acquired through an RS232 connection and a Pc-Eye (Eltec, Germany) RGB frame grabber. Due to the high image acquisition rate, only 360 images could be acquired at a time (limited by the frame grabber). This yielded 6 s time series at the maximum sampling rate (60 Hz) and a 60 s time series with a 6 Hz image rate. The footprint on the surface was 36.8 cm in the along-wind direction and 27 cm in the cross-wind direction giving a resolution of $\Delta x = 0.0557$ cm and $\Delta y = 0.1123$ cm (Nyquist of 5640 rad m^{-1} and 2797 rad m^{-1}, respectively). Finally, the analog video signal was also acquired for synchronization with the infrared camera.

2.2.2. *Surface infrared system*

The surface temperature was monitored with an infrared camera (Galileo, Raytheon-Amber, Goleta, CA), having 256×256 elements, sensitive to wavelengths between 3 μm and 5 μm; imaging at 60 Hz, 12-bit resolution with a 1.22 ms integration time. The camera was mounted to view the surface through a sealed aperture in the roof of the wind-tunnel section at a small angle of incidence to avoid imaging the reflection of the cold lens in the surface and to avoid interference with the CISG (figure 1). Prior to the experiments, an external temperature calibration was performed using a well-mixed cold-water bath having a temperature accurate to 0.01 K. In all cases, our calibration was consistent with the manufacturer's calibration, and within the specified noise level of 0.015 K. Note that at a wavelength of 3–5 μm, the penetration depth of the radiation is on average 7.75 μm (Downing & Williams 1975), so the IR camera is sensing the temperature of a layer of water $O(10)$ μm thick. This penetration depth is considerably smaller than the typical thermal boundary layer (1–30 mm). Therefore the temperature recorded by the infrared camera is the temperature of the surface skin layer. The digital data from the camera were acquired using a IC-PCI 2.0 frame grabber and the AMDIG-16D-HS digital acquisition module (Imaging Technology, Bedford, MA) synchronized with the CISG. The data were acquired in blocks of 1800 frames at either 60 Hz or 30 Hz giving time sequences 30 s or 60 s long, respectively. The footprint of the camera was 40 cm × 40 cm, enclosing the footprint of the CISG system to give coincident, simultaneous measurements. This image size gives a resolution of $\Delta x = \Delta y = 0.156$ cm (Nyquist of 2014 rad m^{-1}).

In order to measure the surface velocity, an infrared CO_2 laser (Model 48-2, Synrad, Mukilteo, WA) was used to scan a thermal linear marker onto the water surface at 2 Hz. This thermal marker, of 1 cm width, with an initially Gaussian temperature distribution, could then be imaged with the IR camera to give the velocity of the marked fluid. With a wavelength of 10.6 μm, the penetration depth of the radiation is 11 μm (Downing & Williams 1975). This method of measuring the surface velocity was chosen because it does not require seeding the surface with particles that can affect

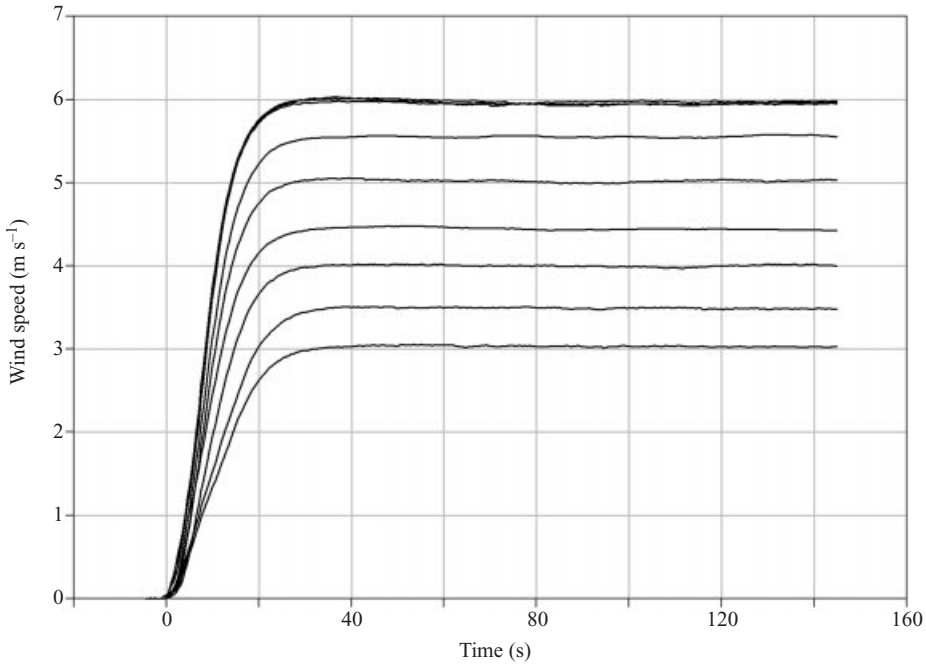

FIGURE 2. Time series of the wind speed for all tested conditions. Also shown are time series of the wind speed for three typical runs with a final target wind speed of 6 m s^{-1} which illustrate the good repeatability in the wind acceleration and final speed.

the surface tension. Care was taken in verifying that the elevated surface temperature induced by the laser was not of dynamical significance.

2.2.3. *Wave height and wind speed measurements*

During the experiments, time series of the wind speed and wave height were sampled at 200 Hz using a 12-bit data acquisition card (DAQ 1200, National Instruments, Austin, TX). The same A/D board was used both to send the signal to the hydraulic system that controls the fan of the wind tunnel, and to generate a trigger for instrument synchronization. The wind speed was measured using a Pitot-static tube connected to a Baratron pressure transducer (310BH-10 MKS Instruments, Andover, MA). The total pressure port of the Pitot-static tube was placed at the centreline of the wind tunnel (59.5 cm from the water level), 48 cm upstream of the centre of the CISG. The wind speed in the wind tunnel is dependent on both the voltage sent to the hydraulic valve and the water level. Due to the modifications to the wind tunnel, a complete calibration of the valve response was performed.

The surface displacements were measured with a resistance-wire wave gauge constructed of a pair of thin nichrome wires (0.015 cm diameter) separated by 0.3 cm. The wave gauge was placed at $y = -53.0$ cm, away from the centreline in the cross-wind direction and aligned with the centre of the frame of the CISG. The signal was sent to a Danish Hydraulic Institute electronic amplifier prior to sampling. The wave gauge was calibrated at the beginning and end of each day's experiments. Any DC drift from run to run was subtracted using the first 4 s of quiescent data from each run.

2.3. *Procedure*

At the beginning of a day's experiments, the surface was skimmed, the surface level was checked and adjusted if necessary, and then the wind was blown continuously for 30 minutes at about $8\,\mathrm{m\,s^{-1}}$ to warm up the hydraulic system and to sweep the remaining surface film towards the beach end of the facility. The channel was then allowed to settle for 30 minutes during which time a wave gauge calibration was performed, and the air and humidity temperature inside and outside the wind tunnel were measured, along with the atmospheric pressure. At this time, the final preparations for the image acquisition computers were completed. The experiments were conducted at night, in the dark. This permitted consistent light conditions for the CISG and a favourable heat flux from the water to the air which yielded good temperature contrast between the surface skin layer and the bulk of the water. For each run, the wind was smoothly increased from rest to its final value in 20 s (figure 2). Typically, a run lasted for 150 s during which time the wind speed and wave height were continuously sampled. Experiments were conducted for final wind speeds of 3, 3.5, 4, 4.5, 5, 5.5 and $6\,\mathrm{m\,s^{-1}}$ at a fetch of 10.72 m and for wind speeds of 3, 4, 5 and $6\,\mathrm{m\,s^{-1}}$ at all other fetches.

Further experimental details can be found in Veron (2000).

3. Results

3.1. *Flow visualization*

As described in the preceding section, the wind is accelerated from rest to a final value between 3 and $6\,\mathrm{m\,s^{-1}}$ in approximately 20 s. The wind speed is the only controlled input and the flow in the water evolves naturally under the influence of the kinematical and dynamical effects of the wind. Visualization of the surface flow with the IR camera and the CISG permits a description of the evolution of the waves and surface velocity during the experiment. In each run, the stress due to the increasing wind speed accelerates the surface of the water. During this early stage of the flow, momentum is transferred to depth by viscous diffusion (Melville *et al.* 1998) and a laminar boundary layer develops in the water below the interface.

The surface then becomes unstable to surface-wave modes. Figure 3 shows the along-wind and cross-wind slope of the surface wave field at $t = 17$, 25, 34 and 50 s for a final wind speed of $5\,\mathrm{m\,s^{-1}}$ at a fetch of 10.72 m. At $t = 34$ s, the waves show some sign of nonlinearity (slope and curvature effects) as parasitic capillary waves appear on the front face of the dominant gravity waves (Cox 1958; Longuet-Higgins 1995; Fedorov & Melville 1998). Shortly after the generation of the first waves, the surface flow becomes unstable and develops Langmuir circulations (cf. Melville *et al.* 1998).

Streaks become apparent in the thermal images (figure 4) which exhibit regions of surface convergence and divergence associated with local surface jets and wakes, respectively. In figure 4, the vertical (cross-wind) warm lines are the thermal markers laid down by the scanning beam of the CO_2 laser. The surface jets, subjected to an increasing shear, eventually become unstable as well and the flow evolves into fully developed turbulence. These four stages in the evolution of the surface flow were also observed in the experiments of Melville *et al.* (1998) and are common to all tested wind speeds. In summary, they are:

1. uniform and monotonic acceleration of the surface;
2. wind wave generation and growth;

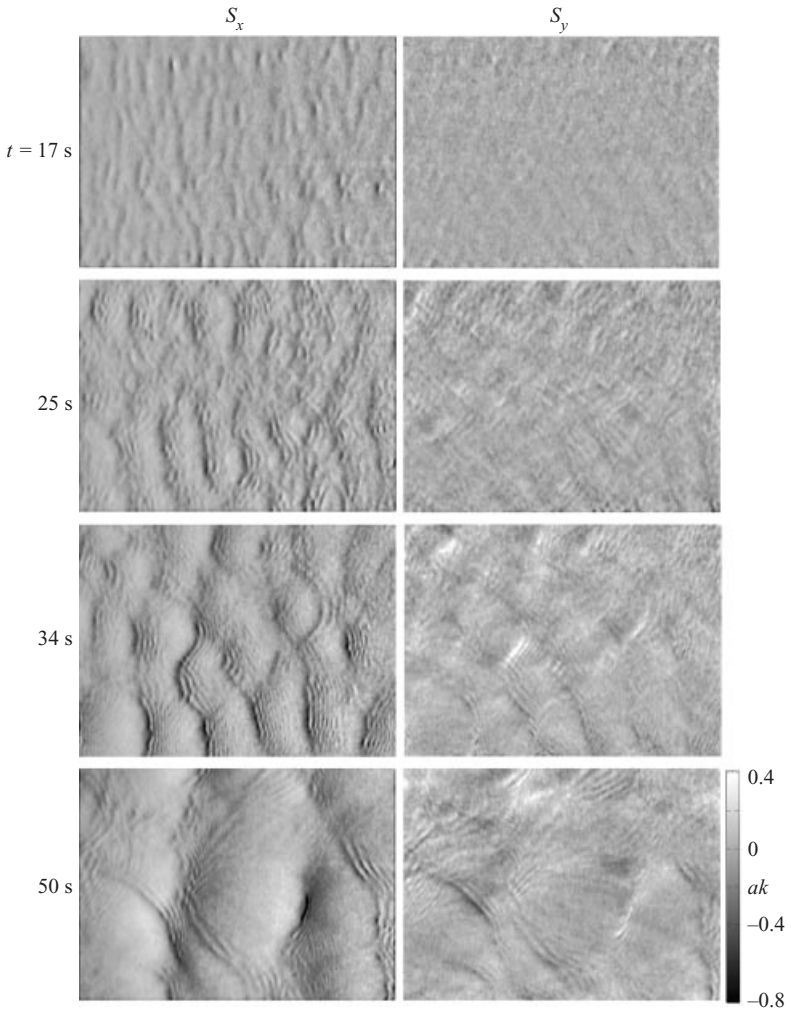

FIGURE 3. Along-wind slope, S_x, and cross-wind slope, S_y, of the surface wave field at $t = 17$, 25, 34 and 50 s for a final wind speed of 5 m s^{-1}, at a fetch of 10.72 m. Image size is 36.8 cm by 27 cm. The wind is blowing from left to right.

3. Langmuir circulation generation and evolution:
   generation of high velocity jets (streaks) separated by low velocity wakes;
   jet bifurcation and dislocation;
   transition to turbulence;
4. fully developed turbulence.

Figure 5 shows the surface temperature field for final wind speeds of 3, 4, 5 and 6 m s^{-1} at a fetch of 10.72 m and at similar stages in the evolution of each flow. Clearly, the length scale of the Langmuir cells diminishes with increasing wind speed. In addition, the time scale to reach each stage also decreases with increasing wind speed. At higher wind speeds, the first signs of Langmuir circulations appear sooner, and the period of high coherence before the transition to turbulence is shorter.

3.2. *Surface waves*

3.2.1. *Wave height*

Figure 6 shows a frequency spectrogram of the surface displacement recorded with the wire wave gauge for a final wind speed of $5\,\mathrm{m\,s^{-1}}$ at a fetch of 10.72 m. It is calculated with 1 s windows having 50% overlap. Due to the limited frequency response of the wire wave gauge (less than 50 Hz say), the spectrogram is shown for frequencies lower than 30 Hz. The first detectable waves appear at approximately $t = 20\,\mathrm{s}$ at a frequency of 14 Hz. With time, the peak frequency of the wave field shifts to a lower value, as the waves evolve from a duration-limited to fetch-limited state (figure 6). The peak then stabilizes around 4 Hz. During that time, the peak spectral density rises to a final value of approximately $4 \times 10^{-2}\,\mathrm{cm^2\,Hz^{-1}}$. Figure 6 compares very well with the data of Melville *et al.* (1998). Cuts through the spectrogram shown in figure 6 yield individual spectra of the surface wave displacement (figure 7). Each spectrum is computed for a 4 s window (average of 4 cuts through the spectrogram) centred on the time shown. The spectra compare very well with those of Kawai (1979, figure 10), who measured surface wave height spectra for a wind speed of $5.1\,\mathrm{m\,s^{-1}}$, at an 8 m fetch. Also, figure 7 shows, as expected, that the wave stabilizes at a peak frequency that decreases with increasing fetch. At $t = 10\,\mathrm{s}$, the spectrum shows that the noise level of the system lies around $10^{-7}\,\mathrm{cm^2\,Hz^{-1}}$, and exhibits two noise peaks at 6.3 Hz and 12.6 Hz. They are believed to be due to vibration of the arm of the wave gauge when exited by the wind-tunnel fan.

3.2.2. *Wave slope*

Figure 3 shows the evolution of the surface slope components, S_x and S_y for a final wind speed of $5\,\mathrm{m\,s^{-1}}$ at a fetch of 10.72 m. As for the wave gauge data, the slope data show the downshift of the dominant surface wavenumber as the wave field grows. Figure 8(*a*) is the spectrogram of the along-wind slope S_x shown in figure 3, taken in the along-wind direction. It is constructed by taking spectra of S_x in the x-direction for the 240 lines (y-direction) of the slope image. The 240 resulting spectra are then averaged, yielding a single wavenumber spectrum for S_x. The operation is repeated for the 360 slope images acquired at a 6 Hz rate. Figure 8 shows that the first detectable waves appear at approximately $t = 15\,\mathrm{s}$ with a wavelength of 2.6 cm. As in figure 8 the peak of the spectrogram downshifts with time indicating an increase in wavelength of the carrier waves. However, there is not a clear indication of the transition between the duration- and fetch-limited regimes. Integrating the spectrograms with respect to the wavenumber yields time series of the surface slope variance for both S_x and S_y (figure 8*c*). The variance of the surface slope increases exponentially from $t = 15\,\mathrm{s}$ until $t = 18\,\mathrm{s}$, the time at which Langmuir circulations first appear (figure 4). For $t > 18\,\mathrm{s}$ the variance of the surface wave slope increases, albeit with large fluctuations, especially for $t > 40\,\mathrm{s}$, the time at which the fetch-limited state is evident in figure 6. Again, there is no sign of a clear transition between the fetch- and duration-limited regimes. The large variations in the record for $t > 40\,\mathrm{s}$ are due to the poor statistics, as the surface wavelength becomes comparable with the image size of the CISG. This can also be seen in figure 8(*a*) where the spectral peak approaches the resolution of the system for larger times.

Figure 9 shows the directional saturation spectra $B(\theta, k)$, averaged from $t = 45$ to 55 s, for S_x and S_y at a $5\,\mathrm{m\,s^{-1}}$ wind speed and a fetch of 10.72 m. The saturation

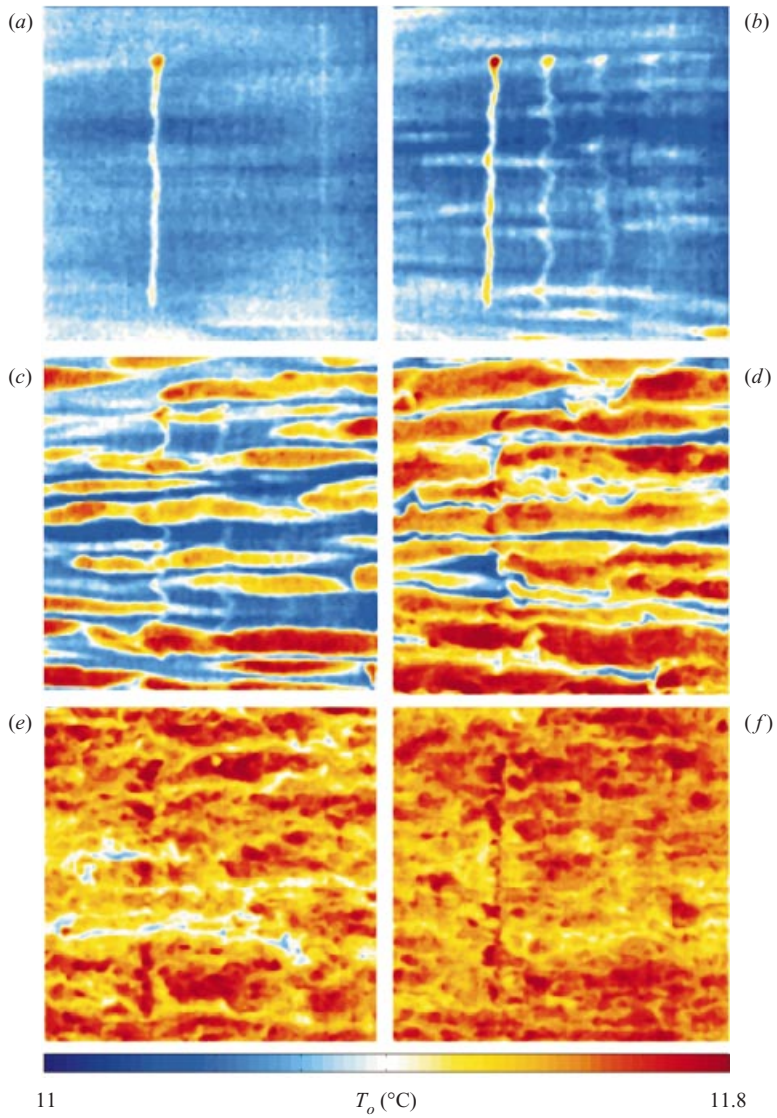

FIGURE 4. Surface temperature field for a final wind speed of 5 m s^{-1}, at a fetch of 10.72 m. Times shown are 16.8, 18.3, 19.8, 21.3, 22.8 and 24.3 s (*a–f*). Image size is 40 cm by 40 cm. The vertical wavy lines are the thermal markers laid down by the scanning CO_2 laser. The temperature is given by the colour code in degrees Celsius.

spectrum, or degree of saturation is defined by Phillips (1985) as

$$B(\boldsymbol{k}) = k^4 F(\boldsymbol{k}) \tag{3.1}$$

where $F(\boldsymbol{k})$ is the wave height spectrum. The spectra are shown in a similar coordinate system to those of Jähne & Riemer (1990) and Klinke (1996). They exhibit a bi-modal shape, with the lowest peak being due to the long surface gravity waves having a wavelength of approximately 12.5 cm, as observed in figure 3. The second peak at around 800 rad m^{-1} corresponds to a wavelength of 0.78 cm and is believed to be caused by parasitic capillary waves riding on the longer gravity waves (cf. Ebuchi,

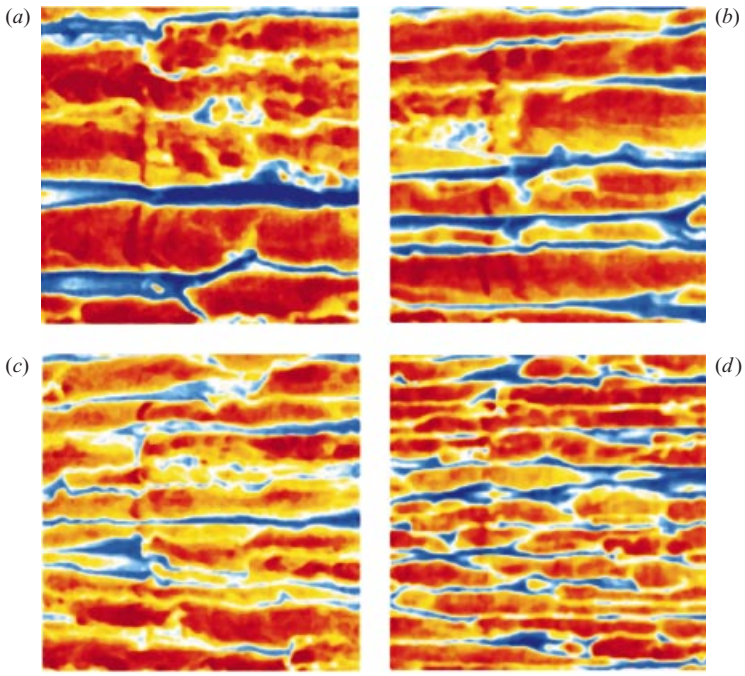

FIGURE 5. Surface temperature fields for final wind speeds of (*a*) 3, (*b*) 4, (*c*) 5, and (*d*) 6 m s^{-1} at a fetch of 10.72 m and at similar stages in the evolution of the flow. Times shown are 43.8, 28.3, 21.3 and 14.3 s, respectively.

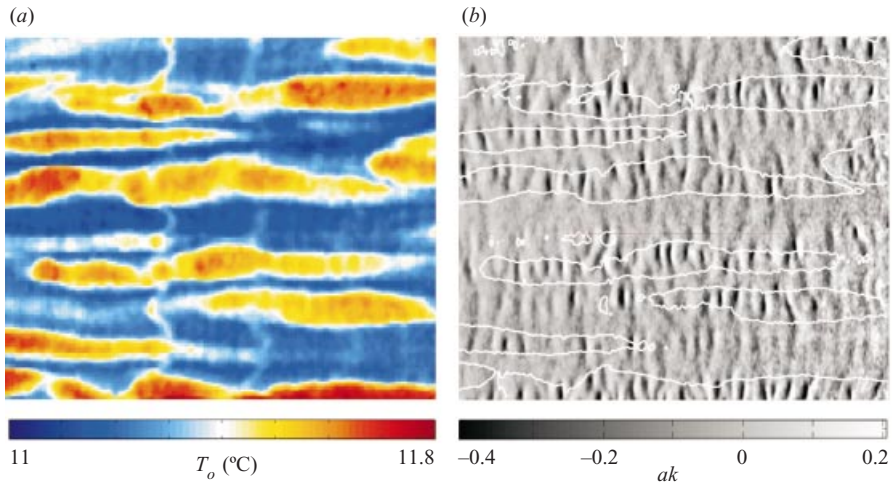

FIGURE 15. (*a*) Surface temperature (from figure 4*c*), and (*b*) along-wind slope at the same location at time $t = 19.8$ s. Note the correlation between the warm upwelling regions and the regions of larger wave slope. Wind and waves are travelling left to right. The image size is 36.8 cm × 27 cm.

Kawamura & Toba 1987). The dip at $k \simeq 360$ rad m^{-1} separating the two peaks thereby separates the gravity and the capillary wave regimes. The Bond number, Bo, gives the ratio of surface tension forces to gravity,

$$Bo = \frac{\gamma k^2}{\rho g}, \tag{3.2}$$

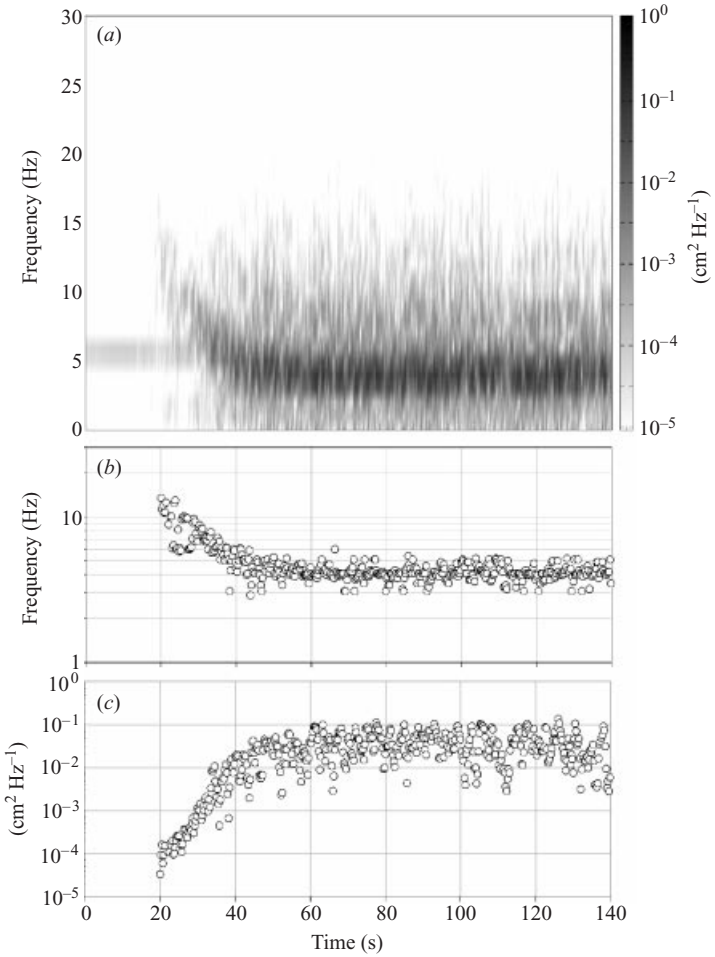

FIGURE 6. (*a*) Spectrogram of the surface displacement recorded by the wire wave gauge for a final wind speed of 5 m s^{-1} at a fetch of 10.72 m. The band at 6 Hz is noise introduced by vibrations of the mounting arm for the wave gauge excited by the fan. It is approximately four to five orders of magnitude lower than the spectral peaks. (*b*) Time evolution of the peak frequency, and (*c*) the peak energy density.

with a Bond number of unity yielding the wavenumber at which gravity and surface tension are equally important:

$$k_m = \left(\frac{\rho g}{\gamma}\right)^{1/2} = 360\,\mathrm{rad\,m^{-1}}, \tag{3.3}$$

where γ is the surface tension, ρ the density of water, and g the acceleration due to gravity. This scale also corresponds to the waves with the minimum phase speed. As shown in figure 9 the dip in the wavenumber slope spectra lies at the scale given by a Bond number of unity. This was previously observed by Zhang (1995), who also noted that the dips, or valleys, fill in at higher wind speeds ($> 8\,\mathrm{m\,s^{-1}}$). The data also show that, as expected, the waves in the along-wind and cross-wind slope images mainly propagate in the x- and y-directions, respectively. In this case, the waves with slopes in the cross-wind direction appear to primarily propagate at 40–50° from the

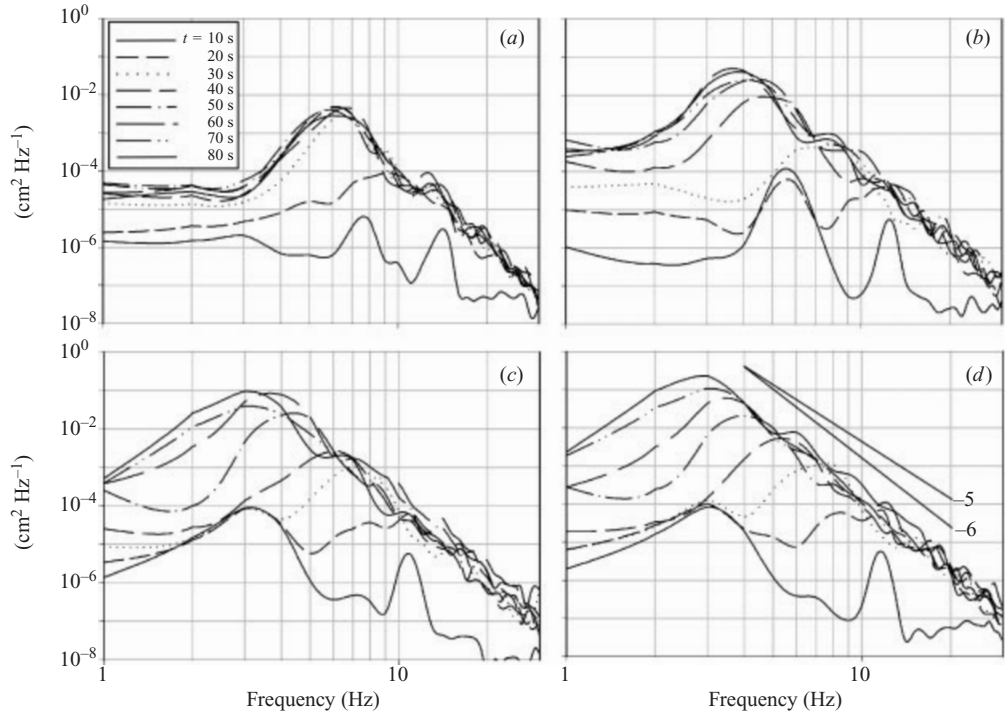

FIGURE 7. Spectra of the surface displacement calculated over 4 s of data centred at the time shown for a final wind speed of 5 m s^{-1} for fetches of (*a*) 4.6, (*b*) 10.72, (*c*) 15.62, and (*d*) 19.29 m. $t = 10$ s shows the noise level of the system.

wind direction. The directional saturation slope spectra compare well with those of Jähne & Riemer (1990).

3.2.3. *Initial scales*

As seen in the previous section, both the wave field and the flow develop with time. Of particular interest are the scales of the waves that are first observed. The CISG yields such information and we present it here for completeness. Table 1 shows the initial wave parameters for the first detectable waves.

The data shown in table 1 compare favourably with those of Kawai (1979); however, some caution is advised. Kawai's experiments were designed to study the initial generation of waves where wind stress was rapidly increased to a constant value in order to be easily modelled by a step function. Thus, the shear layer in the water could be approximated by a similarity solution corresponding to a constant stress at the surface. The experiments presented here were designed to study the instability of the flow to Langmuir circulations that accompany the generation of the waves. In these experiments, the wind stress cannot be approximated by a step function and the resulting flow in both the air and the water are driven by time-dependent surface boundary conditions.

3.3. *Surface velocity – momentum boundary layer*

3.3.1. *Evolution of the surface velocity: measurements*

As described earlier, the flow evolves in four stages from the initial acceleration and deepening of the surface shear layer which becomes unstable to surface waves and

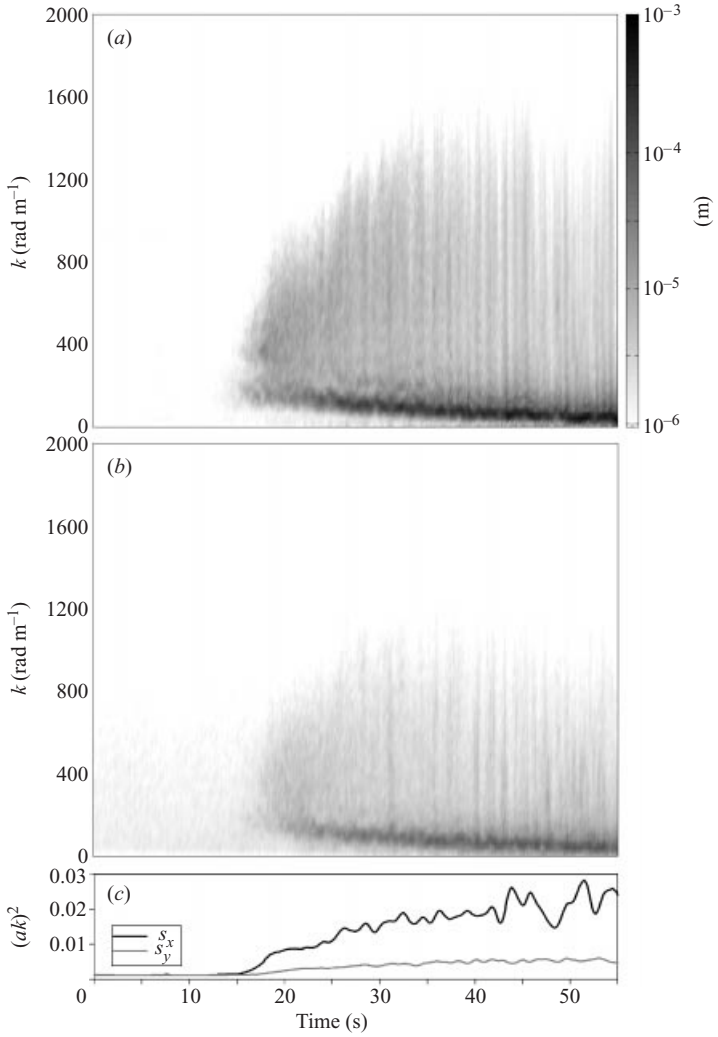

FIGURE 8. Spectrograms of the surface slope for (*a*) S_x and (*b*) S_y, where individual spectra are taken in the along-wind direction. The data shown are for a final wind speed of $5\,\mathrm{m\,s^{-1}}$. (*c*) Integrated spectrogram showing the time evolution of the surface slope variance.

subsequently to Langmuir circulations. The Langmuir circulations initially appear as streaks that are easily visualized by the IR camera through the temperature difference between the surface skin layer and the bulk of the fluid (Katsaros 1980). The surface skin layer of the water surface, also referred to as the 'cool skin' is typically $O(0.1\,\mathrm{K})$ colder than the bulk of the water. Our high-resolution IR camera permits the visualization of the temperature difference between the cool skin and the bulk of the fluid. Regions of surface convergence and divergence associated with local surface jets and wakes, respectively, are also clearly apparent. Figure 4 shows the surface temperature for a final wind speed of $5\,\mathrm{m\,s^{-1}}$ at a fetch of 10.72 m. From the distance between two thermal markers left by the scanning CO_2 laser, or the displacement of the marker during a known time, it is possible to accurately measure the fluid velocity at the surface.

Figure 10 shows the result of the measured surface velocity, $U_o(t)$, for the data

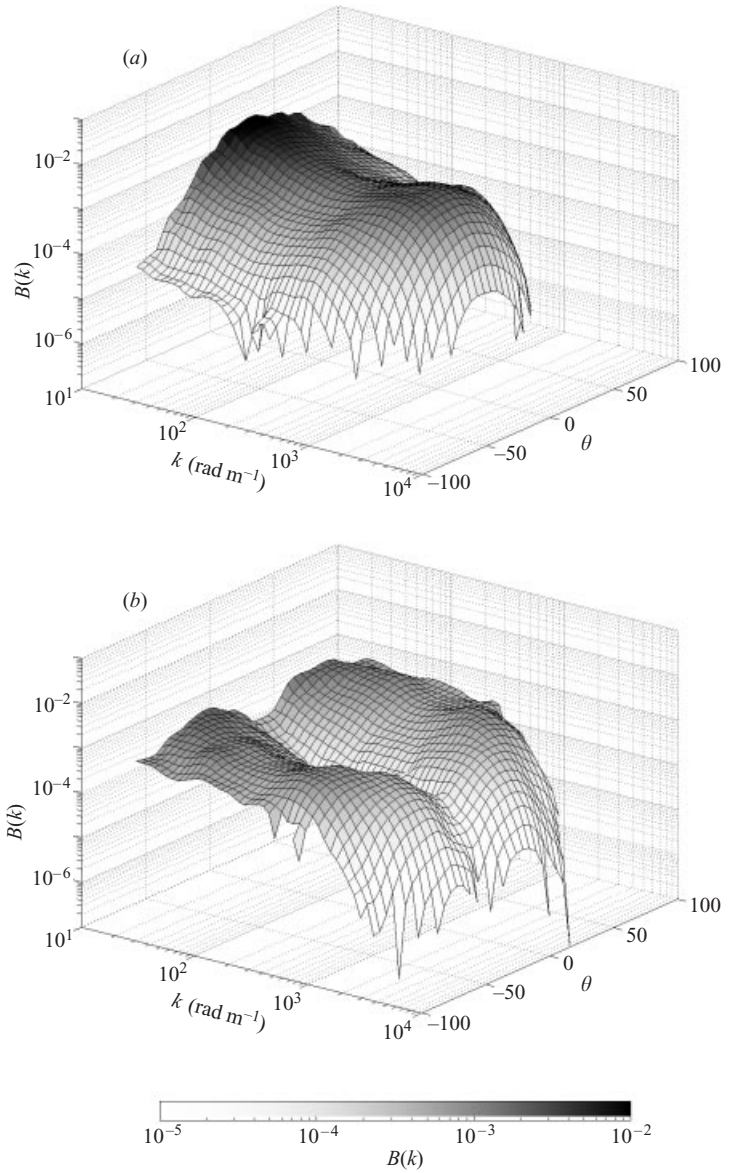

FIGURE 9. Directional saturation slope spectra $B(\theta, k)$ for (*a*) S_x and (*b*) S_y for a final wind speed of 5 m s^{-1} at a fetch of 10.72 m. The angle of propagation θ is taken with respect to the along-wind direction x.

of figure 4. Following a starting transient lasting approximately 5 s, the surface accelerates uniformly until approximately $t = 18.3$ s, at which time it shows significant signs of cross-wind velocity as warm regions begin to open up. The linear thermal marker on the surface distorts, indicating regions of fast downwind motion, or jets, and regions of slower motion, or wakes. At $t = 19.8$ s, the Langmuir circulations appear clearly as a series of along-wind streaks. The surface thermal markers allow the separate measurement of the velocity of the jets and wakes. Shortly thereafter, the regions of increasing shear between the jets and the wakes develop instabilities and the entire flow evolves into a turbulent regime. Once the flow is turbulent, the

Final wind speed ($m\,s^{-1}$)	Time (s)	Wavelength λ_w (cm)	Frequency f_w (Hz)	Phase speed c ($cm\,s^{-1}$)
3.0	32.1	4.19	6.60	27.7
3.5	26.5	3.59	7.31	26.3
4.0	20.8	3.39	7.60	25.8
4.5	18.5	2.79	8.78	24.6
5.0	16.5	2.56	9.40	24.1
5.5	13.2	2.28	10.45	23.7
6.0	12.0	2.09	11.28	23.4

TABLE 1. Measured surface-wave wavelength, λ_w, and frequency, f_w, at the time of the first detectable waves. The phase speed c, relative to the current, is calculated using λ_w and the linear dispersion relationship for gravity–capillary waves.

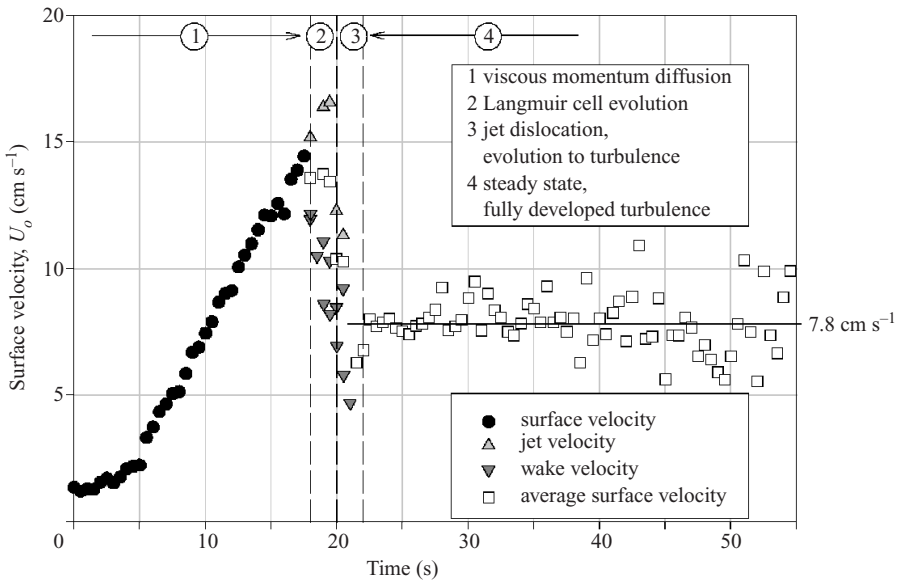

FIGURE 10. Evolution of the surface velocity, $U_o(t)$, measured from the displacement of the surface thermal marker for a final wind speed of $5\,m\,s^{-1}$ and a fetch of 10.72 m. The four stages of the evolution of flow are clearly identifiable.

surface velocity can no longer be segregated into jets or wakes, and the average surface motion appears to stabilize at a somewhat lower velocity indicating that the Langmuir circulations have mixed down the momentum initially provided by the wind to the thickening shear layer. In addition, once the waves are well developed, the Stokes drift adds to the Lagrangian surface velocity, and to turbulent fluctuating velocities that are measured after the breakdown of the circulations. Note, however, that in figure 4, larger-scale longitudinal structures are still visible for $t > 22.8$ s and can be enhanced by coherent averaging. It is evident from figure 10 that the Langmuir circulations have efficiently and rapidly mixed down a large fraction of the momentum provided by the wind to the uppermost layers of the fluid (cf. Melville *et al.* 1998).

3.3.2. *Time and length scales at instability*

Continuous imaging of the surface with the IR camera yielded the time at which the Langmuir circulations were first observed, the length scale of the cells, and the surface

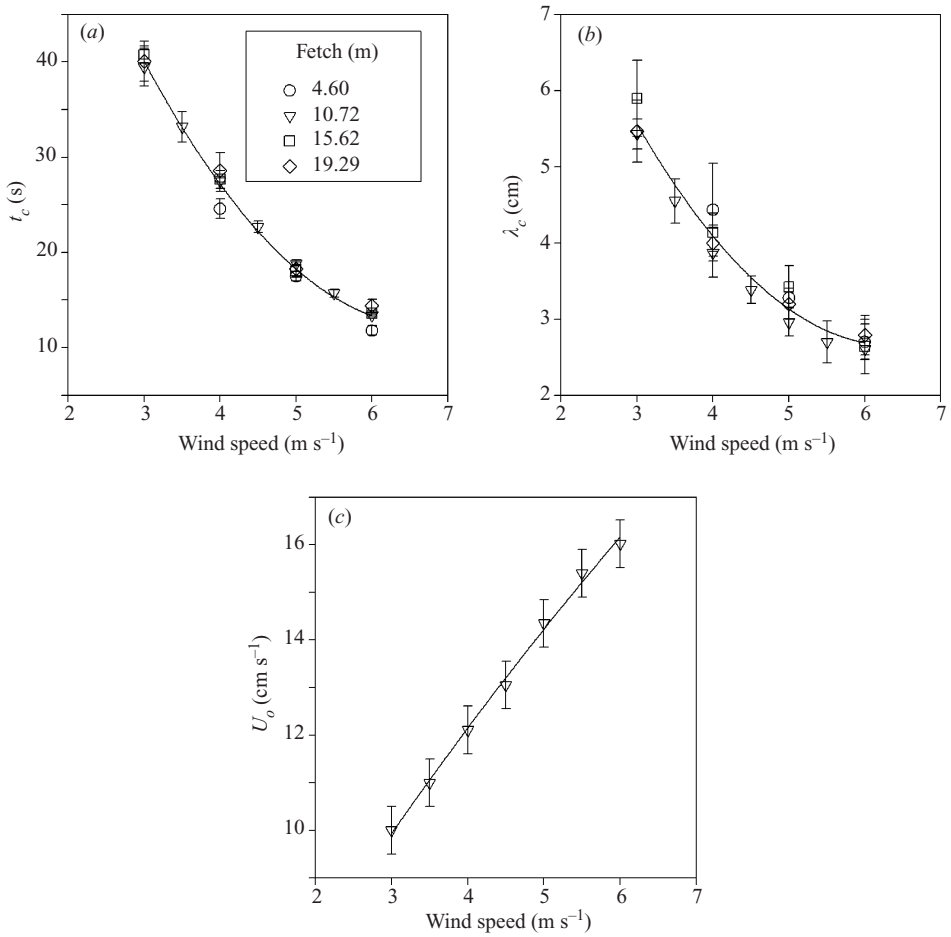

FIGURE 11. (*a*) Time, (*b*) spanwise wavelength, and (*c*) surface velocity at the inception of the instability, as a function of the final wind speed.

velocity at the inception of the instability. Figure 11 shows the relevant scales averaged over an ensemble of 4 runs. The error bars are the standard deviation of the ensemble. The time at which the instability is first observed as well as the sizes of the initial cells decrease, and the surface velocity increases, with increasing final wind speed (see also figure 4). Note however that in figure 4 the larger-scale longitudinal structures are still visible for $t \geqslant 22.8$ s. Figure 12(*a*) shows a three-dimensional representation of the surface temperature where a single cross-wind cut though the surface temperature images provides an x, t temperature image (figure 12*b*). From figure 12(*b*), it is apparent that the transition to turbulence thought the development of the Langmuir circulations is accompanied by an inverse cascade of the cross-wind scales. Furthermore, although the surface flow is fully turbulent, longitudinal coherent structures remain embedded in the flow. This is emphasized by a 20 s ensemble average of the surface temperature starting at $t = 20$ s (figure 12*c*), which clearly shows cross-wind surface temperature variations associated with the longitudinal structures in the flow.

In addition to the surface parameters provided by the thermal data, the CISG and wave gauge provided the surface-wave parameters at the inception of the Langmuir circulations. Table 2 summarizes those results.

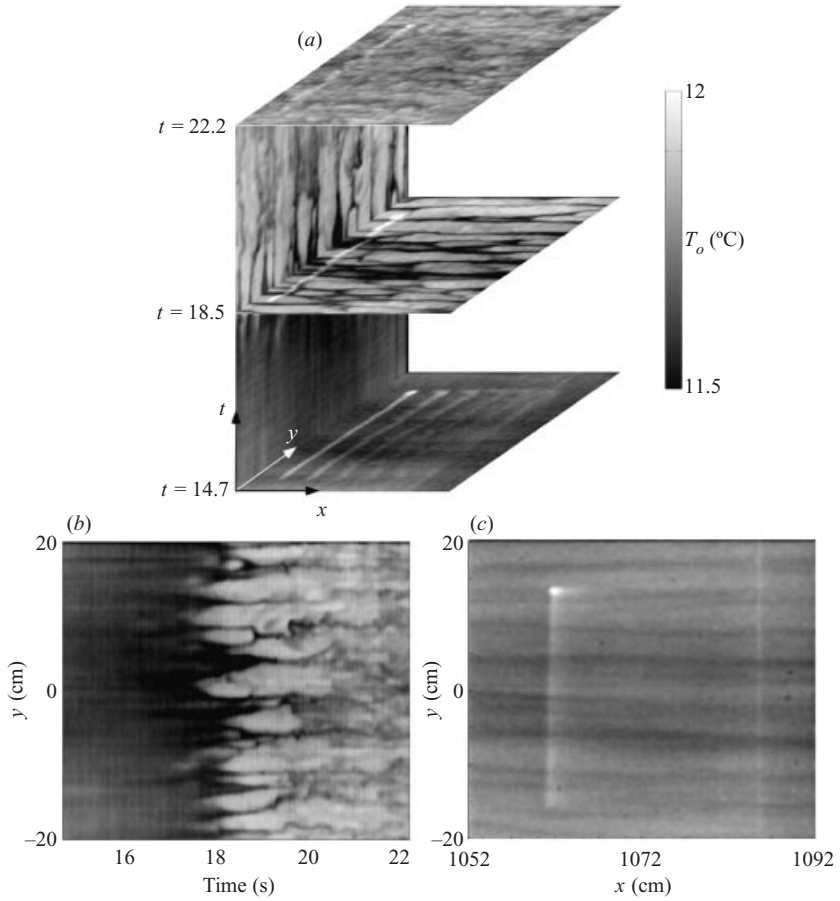

FIGURE 12. (*a*) Three-dimensional representation of the surface temperature. The horizontal images (x, y) are similar to those of figure 4. The vertical axis shows a cross-wind cut though the surface images with time. (*b*) The x, t image obtained by taking a cross-wind cut with time of the surface images. (*c*) 20 s average of the surface temperature starting $t = 20$ s (after turbulent transition). Note that the cross-wind structure is still clearly visible. Data shown are for a $5\,\mathrm{m\,s^{-1}}$ final wind speed at a fetch of 10.72 m.

3.4. *Surface temperature – thermal boundary layer*

3.4.1. *Evolution of the surface temperature: measurements*

From figures 4 and 10 and our earlier work (Melville *et al.* 1998; Veron & Melville 1999*b*) it is clear that Langmuir circulations disrupt the momentum boundary layer and lead to rapid mixing of the surface layer. Consequently, Langmuir circulations will also affect the surface thermal boundary layer. Figure 13 shows the time evolution of the surface temperature, $T_o(t)$, detected by the IR camera and averaged over the portion of the image that is not contaminated by the thermal marker (upwind of the marker). The data shown were taken for a final wind speed of $5\,\mathrm{m\,s^{-1}}$ at a 10.72 m fetch. It shows a similar evolution to that of the surface velocity. While the wind is accelerating, the surface temperature monotonically drops due to evaporative cooling. When the flow becomes unstable to Langmuir circulations, the underlying warmer fluid is mixed up to the surface while the colder skin layer is rapidly mixed down. The average surface temperature in this particular case increases from 11.1 °C to 11.7 °C

Final wind speed ($m\,s^{-1}$)	Wavelength λ_w (cm)	Frequency f_w (Hz)	Phase speed c ($cm\,s^{-1}$)
3.0	4.30	6.51	28.05
3.5	4.19	6.63	27.78
4.0	3.86	6.98	27.02
4.5	3.39	7.63	25.95
5.0	3.21	7.95	25.51
5.5	2.86	8.67	24.76
6.0	2.38	10.18	23.81

TABLE 2. Measured surface wave parameters at the inception of the Langmuir circulations.

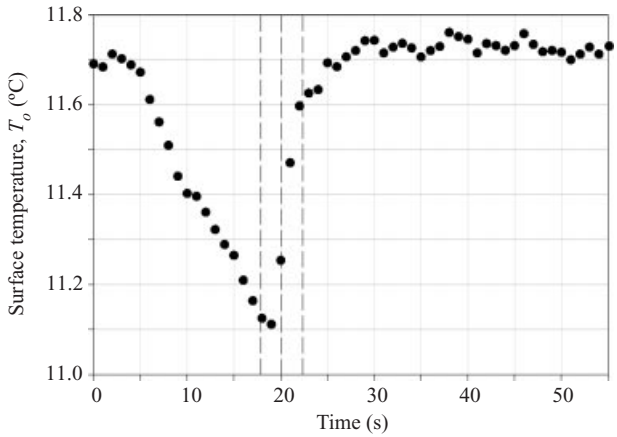

FIGURE 13. Evolution of the surface temperature, $T_o(t)$, measured with the infrared camera, for a final wind speed of $5\,m\,s^{-1}$ and a fetch of 10.72 m.

in about 10 s under the influence of vertical mixing by the Langmuir circulations. A closer examination of the transition at the inception of the Langmuir cells shows that the distribution of the surface temperature is bi-modal during the transition that corresponds to stages 2 and 3 in figure 4: $t = 19.8$–21.3 s. This distribution cannot be reconciled with surface renewal models based on random sub-surface turbulent motion (Haußecker 1996) in which the surface temperature is best represented by a log-normal probability density function. This indicates that the swift renewal of the surface layer by the instability involves coherent kinematical processes that may play an important role in the fluxes of heat and gases at the surface of natural water bodies at low wind speeds. This will be discussed below. It is clear that Langmuir circulations provide a rapid and efficient way of disrupting the thermal boundary layer.

3.5. *Langmuir circulation – surface-wave interaction*

As discussed above, the large fluctuations in the r.m.s. slope for times $t > 40$ s are induced by the limited size of the footprint, and thus the poor statistics, as the surface wavelength becomes comparable to the image size. On the other hand, for $t < 40$ s, the slope images contain a sufficient number of waves to perform Fourier analysis. Figure 14 shows the frequency–wavenumber spectrum for the along-wind slope for 2 s of data starting at $t = 25$ s, for a final wind speed of $5\,m\,s^{-1}$ at a fetch of 10.72 m. Much of the spectrum is in the capillary-wave range ($k > 360\,rad\,m^{-1}$), but compares

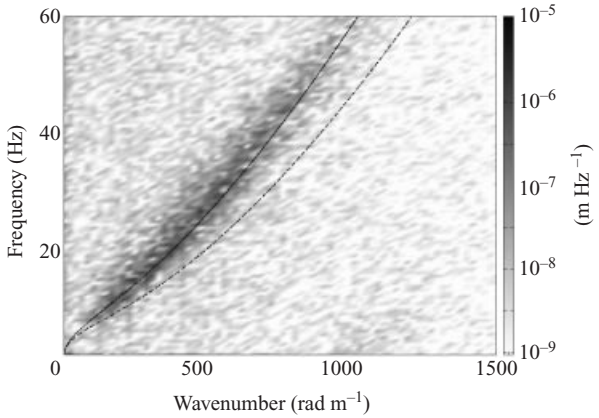

FIGURE 14. Wavenumber–frequency spectrum of the along-wind slope calculated for a final wind speed of 5 m s^{-1}. The dashed line is the dispersion relationship for linear gravity–capillary waves. The solid line is the same dispersion relationship with a uniform surface current of 7.8 cm s^{-1}.

well with the linear dispersion relationship for gravity–capillary waves when account is taken of the measured surface velocity of 7.8 cm s^{-1} (cf. figure 10).

The added current in the dispersion relationship is taken to be uniform whereas we expect the real surface flow to be sheared; however, it appears that this simple advection of the waves describes the observed Doppler shift. Clearly the surface current is influencing the propagation of surface waves. From table 2 and figure 11 it is clear that, at the inception of the Langmuir circulations, the surface velocity is of the same order of magnitude as the phase speed of the waves. In the context of the CL theory, this is $O(1)$ scaling and has both kinematical and dynamical consequences when compared to the $O(\epsilon^2)$ theory that applies to larger-scale ocean waves and currents (Leibovich 1983). It raises the question of whether the horizontal velocity gradients associated with the Langmuir circulations are modulating the surface waves.

Figure 15 (see p. 35) shows the co-located thermal and along-wind slope images while the Langmuir circulations are developing (cf. $t = 19.8$ s in figure 4*c*). A close look at the slope images reveals that the wave field exhibits along-wind bands of steeper waves which appear to be correlated with the warmer regions of the wakes. This increase in slope is consistent with waves propagating on a decelerating current where wave action conservation and geometrical optics lead to a decreases in the wavelength, and an increase in the surface slope. At this stage in the evolution of the Langmuir circulations they are still largely aligned in the along-channel direction. For both images in figure 15 we computed line-by-line averages (in the y-direction) of the temperature and r.m.s. wave slope. We also used correlation techniques to directly measure $(U_o + c)$, the phase speed of the waves including advection by the current. These results are shown in figure 16, along with a plot of the normalized modulation of ak versus that for $(U_o + c)$. It is very clear, and quantitative analysis confirms, that the wave slope and the surface temperature are strongly coherent, as are the wave slope and the wave phase speed, $(U_o + c)$. The modulation is such that in regions of upwelling (warm wakes, slower flow) the wave slope increases and $(U_o + c)$ decreases, and vice versa for the downwelling regions (cooler surface water, faster flow). The use of the active IR imaging to measure the surface velocity over a restricted region of the image shows that much of the modulation of $(U_o + c)$ is due to the modulation of U_o alone, with U_o varying by up to 5 cm s^{-1} for the

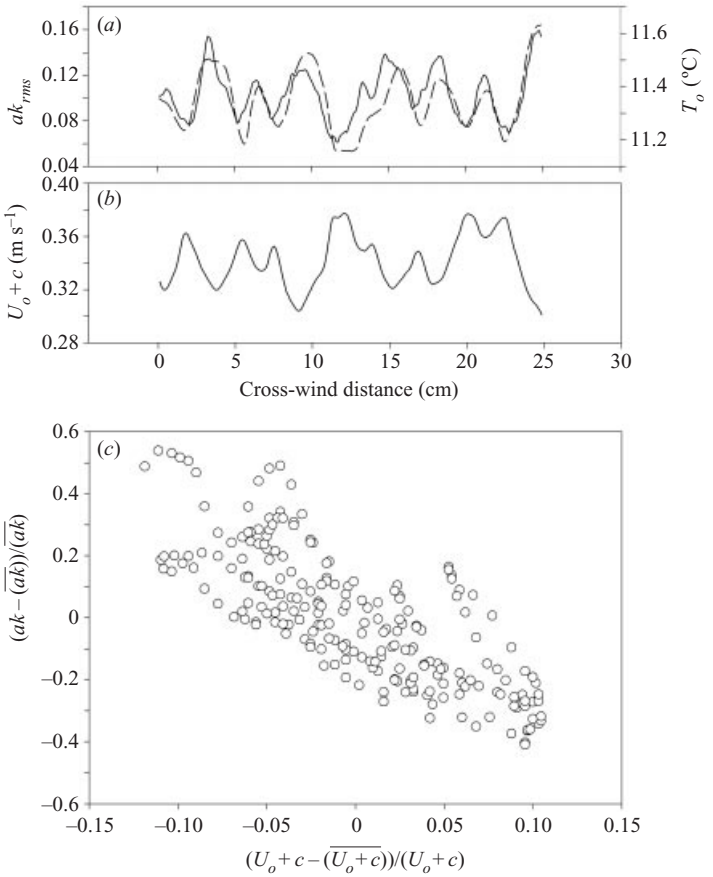

FIGURE 16. Cross-stream modulation of wave slope, ak, the surface temperature T_o, and the surface wave phase speed, $U_o + c$, from figure 15: (*a*) r.m.s. slope (solid line) and mean temperature (dashed line); (*b*) mean phase speed, $U_o + c$, averaged along the streamwise direction of the images; (*c*) deviation of the wave slope versus the deviation of the phase speed, where the overbar represents the cross-stream average.

data shown in figure 16. Prediction of the modulated slope based on homogeneous, stationary, wave action conservation successfully describes the phase of the cross-wind modulation of the waves and captures the qualitative effect of the wakes and jets induced by the Langmuir circulations. The amplitude of the slope modulation, however, is underestimated by approximately a factor of 2. This may be attributed to the fact that assumptions of stationarity and homogeneity do not strictly apply and these effects need to be incorporated. Also, it has been suggested that the lateral divergence of the cross-wind currents might account for part of the observed difference (M. S. Longuet-Higgins, personal communication). This rapid transition to three-dimensional wave patterns in the early stage of the wave generation indicates that two-dimensional models for wind-wave generation might apply only in the very early stages of wave growth. It is apparent that both the classical wave generation problem and the instability of the shear flow to Langmuir circulations are coupled. This renders both phenomena quite complicated and suggests that direct numerical simulations (DNS) or other numerical approaches might be necessary to obtain satisfactory comparison with the experimental data.

3.6. *Fetch dependence*

In addition to experiments for the seven final wind speeds from 3 to 6 m s^{-1} in steps of 0.5 m s^{-1} at a fetch of 10.72 m, we also conducted experiments at fetches of 0.93, 4.60, 10.72, 15.62 and 19.29 m for final wind speeds of 3, 4, 5 and 6 m s^{-1}. Figure 7 above shows the dependence of the wave height spectra on the fetch when the wave field is fetch limited ($t = 80$). It shows that the energy contained in the wave field increases with fetch for a given wind speed. Also, at a given wind speed the peak frequency of the wave spectrum decreases with increasing fetch. Figure 11 shows the time of the inception of the Langmuir circulations t_c, and the wavelength of the cells, λ_c, as a function of the fetch. The measurements show that λ_c is independent of fetch over the range of fetches measured. The time t_c also appears almost independent of fetch with perhaps a slight increase as the fetch increases. This was confirmed by visualizing the entire wind tunnel with the IR camera placed next to the intake section, looking downstream at a grazing angle. Rapid (approximately 5 m s^{-1}) downstream propagation of the instability was observed. The difference in t_c with fetch remains within the repeatability of the experiment and thus within the uncertainty of the measurements. No Langmuir circulations were observed at the shortest fetch and lowest wind speed (4.60 m and 3 m s^{-1}).

At larger times, when the flow is fully established and in steady state, a region of quasi-steady transition between the laminar and the turbulent flow was observed. Upstream of this region, the surface flow is in the pre-Langmuir circulation regime, and downstream it has evolved into fully developed turbulence as described before. Therefore, it appears that there is a fetch at which the conditions for the instability of the flow are met on a statistically stationary basis and where consequently the streaks develop with fetch rather than time. This streaky, statistically stationary region was previously observed by Caulliez, Ricci & Dupont (1999). However, they did not provide an explanation for the phenomenon and did not relate their observation to a transition in the flow regime associated with the instability of the shear flow to Langmuir circulations. A closer look at the region of transition in the surface flow shows that it is closely correlated with the surface wave field, with a corresponding transition between a flat glassy surface and a wavy surface. This may be an indication that the waves are necessary for the subsequent instability of the surface flow. This is consistent with the lack of time dependence in figure 11 since the observed t_c is well within the duration-limited portion of the experiments where the wave field is independent of fetch. In an attempt to further investigate this possibility, it was decided to perform an experiment where the surface wave generation could be inhibited, or at least delayed, by the addition of surfactant to the water.

3.7. *Influence of surfactant*

The experiment was repeated at a fetch of 10.72 m for final wind speeds of 3, 4, 5 and 6 m s^{-1} with surfactant added to the water. Approximately 1 p.p.m. of Triton X-100, a common organic compound used to reduce surface tension in many applications (Henderson 1998), was dissolved in the water. Figure 17 shows the surface velocity measured for a final wind speed of 5 m s^{-1} along with the data of figure 10, the mean surface temperature deviation, $\Delta T_o = T_o(t) - T_o(t = 0)$, and the variance (over 1 s) of the wave height recorded with the wave gauge, with and without surfactants.

The surface displacement record shows that the addition of the surfactant was successful in inhibiting the generation of the surface waves, at least up to $t = 55$ s. Visual observation confirmed that no waves were present during the time shown. In addition, visualization of the surface flow with the IR camera did not show any

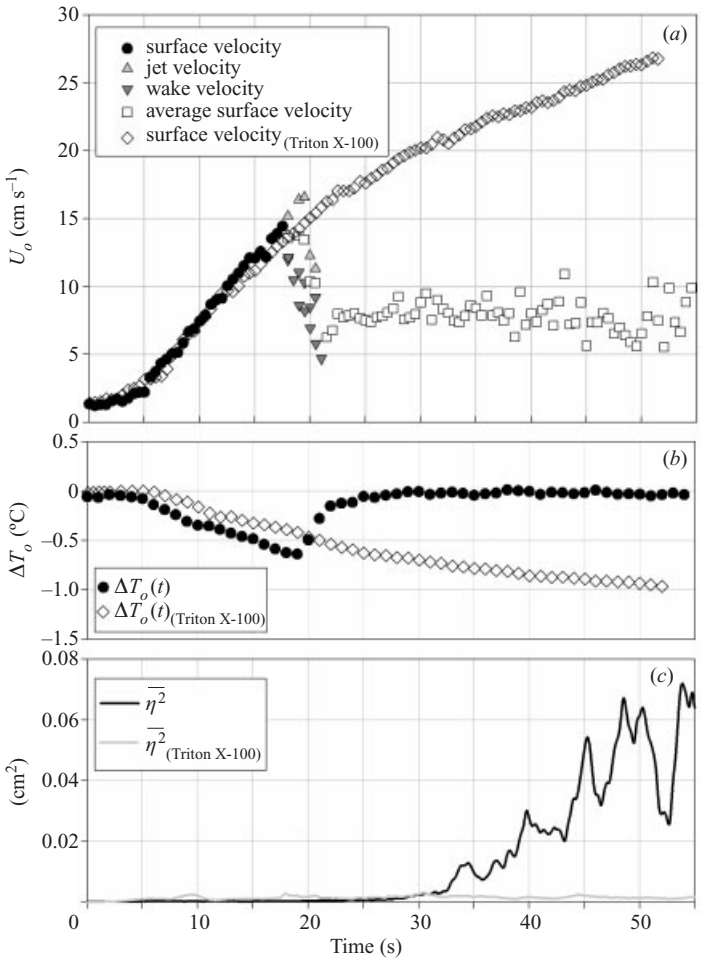

FIGURE 17. (*a*) Surface velocity, (*b*) surface temperature deviation for a final wind speed of 5 m s^{-1} and a fetch of 10.72 m with and without Triton X-100 added to the water (the data of figures 10 and 13 are plotted in (*a*) and (*b*) respectively). (*c*) Shows the time series of the variance of the surface wave height with and without added surfactant.

evidence of Langmuir circulations. Accordingly, the surface velocity continues to increase far past the value of 14.35 cm s^{-1} at $t = 18.8$ s, the time at which Langmuir circulations were observed in the clean water case (figure 10). Similarly, the mean surface temperature shows a monotonic decrease beyond the critical time for the clean water case. The decreasing acceleration of the surface shown in figure 17 is a consequence of the transition from the accelerating wind to the constant final wind speed (see figure 2). The observed surface velocity (with the decreasing acceleration) is consistent with an analytical solution developed in the next section. So, when surfactant is added to the water and surface waves are inhibited, the surface flow appears stable and remains laminar beyond the point of instability for the clean water case. While this result does not preclude the possibility of sub-surface Langmuir circulations, unable to break through the viscous surface layer because of the added surface tension, and therefore invisible to the IR camera, it is hardly conceivable that such circulations would have no detectable influence on the surface velocity. It

is most improbable that the surface velocity would continue to match the laminar solution with a turbulent sub-surface motion. Along with the evidence presented in the previous section, it is concluded that within the range of parameters covered by these experiments, the surface waves are necessary for the instability of the surface flow to Langmuir circulations.

3.8. *Evolution of the surface velocity: theory*

The differences in the evolution of the surface velocity in clean water and that with surfactant, especially the decrease in the acceleration of the surface at longer times in the latter case, prompt us to examine the surface velocity for different temporal evolutions of the surface stress. We consider two-dimensional flow in a semi-infinite water body with a free surface at $z = 0$. The flow is driven by a prescribed surface stress, $\tau(t)$, and is at rest at $t = 0$. Following Melville *et al.* (1998), the governing equation for the mean flow is

$$\frac{\partial u(z,t)}{\partial t} = \nu \frac{\partial^2 u(z,t)}{\partial z^2} \tag{3.4a}$$

with the boundary conditions

$$u(z,t) = 0 \quad \text{for} \quad t \leqslant 0, \tag{3.4b}$$

$$u(z,t) \to 0 \quad \text{as} \quad z \to -\infty, \tag{3.4c}$$

$$\mu \frac{\partial u(z,t)}{\partial z} = \tau(t) \quad \text{at} \quad z = 0. \tag{3.4d}$$

Using the Laplace transform defined by

$$\mathscr{L}(f(t)) = \mathscr{F}(s) = \int_0^\infty \mathrm{e}^{-s\xi} f(\xi)\,\mathrm{d}\xi, \tag{3.5}$$

the stated problem has a solution of the form

$$\mathscr{U}(z,s) = \mathscr{U}_0(s) \exp(z\sqrt{s/\nu}), \tag{3.6}$$

where $\mathscr{U}(z,s)$ is the Laplace transform of the velocity $u(z,t)$, and the integration constant $\mathscr{U}_0(s)$ is the Laplace transform of the surface velocity $U_0(t)$. Evaluating the time-dependent stress at the surface (3.4*d*), gives

$$\mathscr{U}(z,s) = \frac{\mathscr{T}(s)}{\mu}\sqrt{\frac{\nu}{s}} \exp(z\sqrt{s/\nu}), \tag{3.7}$$

where $\mathscr{T}(s)$ is the Laplace transform of $\tau(t)$.

This can be inverted for $u(z,t)$ if $\mathscr{T}(s)$ is specified. We choose here to represent the evolution of the surface stress by a power series in time. This has multiple advantages. It implicitly satisfies the condition (3.4*b*) and also allows us to retain a relatively general form of the solution. Hence, the surface stress

$$\tau(t) = \sum_k \alpha_k t^k \tag{3.8}$$

transforms into

$$\mathscr{T}(s) = \sum_k \alpha_k \Gamma(k+1) s^{-(k+1)} \quad \text{with} \quad k+1 > 0, \tag{3.9}$$

where Γ is the gamma function. Combining (3.7) and (3.9) gives

$$\mathscr{U}(z,s) = \sum_k \alpha_k \Gamma(k+1) s^{-(k+3/2)} \frac{\sqrt{\nu}}{\mu} \exp\left(z\sqrt{s/\nu}\right), \tag{3.10}$$

which is inverted to yield the solution for the velocity in the water,

$$u(z,t) = \sum_k \alpha_k \Gamma(k+1) \frac{\sqrt{\nu}}{\mu} \frac{2^{k+1}}{\sqrt{\pi}} t^{(k+1/2)} \exp(-z^2/8\nu t) D_{-2(k+1)}\left(\sqrt{\frac{z^2}{8\nu t}}\right), \tag{3.11}$$

where D is the parabolic cylinder function. The surface velocity is then

$$U_0(t) = \sum_k \alpha_k \frac{\Gamma(k+1)}{\Gamma(k+3/2)} \frac{\sqrt{\nu}}{\mu} t^{(k+1/2)} = \tau(t) \frac{\Gamma(k+1)}{\Gamma(k+3/2)} \frac{\sqrt{\nu t}}{\mu}. \tag{3.12}$$

If the surface stress has a t^k time dependence, then the surface velocity varies like $t^{k+1/2}$. From equations (3.12) several known results can be retrieved. For example, if $\tau = \alpha_{1/2} t^{1/2}$,

$$U_0(t) = \alpha_{1/2} t \frac{\sqrt{\pi\nu}}{2\mu}, \tag{3.13}$$

and equation (3.11) reduces to

$$u(z,t) = \alpha_{1/2} \frac{\sqrt{\pi\nu}}{2\mu} t \left((1+2\eta^2)\mathrm{erfc}\,(\eta) - \frac{2}{\sqrt{\pi}} \eta \exp\left(-\eta^2\right)\right), \tag{3.14}$$

where $\eta = -z/2(\nu t)^{1/2}$. This particular form is the velocity profile found by Melville *et al.* (1998) to correspond to a linearly accelerating surface velocity.

It is interesting to compare the experimental data on the surface velocity with the theoretical prediction. Figure 18 shows the data of figure 17(*a*) along with the prediction of equation (3.12). In the clean surface case, the velocity accelerates with a $t^{3/2}$ dependence and then rapidly decelerates as the instability occurs. This instability always occurs after the inflection point in the wind speed velocity (figure 2) which allows for the wind speed to plateau (t = 15–20 s). In the case where surfactant is added to the water, two distinct regimes appear. For short times, the measured surface velocity evolves with an approximate $t^{3/2}$ time dependence. According to equation (3.12), this indicates that the surface stress, for short times, can be approximated by a linear function of time. On the other hand, at large times, the surface velocity follows a $t^{1/2}$ dependence, which, according to equation (3.12), implies that the stress is constant. Finally, note here that the two surface velocity regimes mirror the two distinct regimes for the wind: linear acceleration and constant final wind speed.

3.9. *Evolution of the surface temperature: theory*

The surface temperature, like the surface velocity, can be described with a simple diffusion model. We consider the temperature deviation $\Delta T = T(z,t) - T_o(t=0)$. In addition, if we assume that the temperature is uniform with depth at $t = 0$, the governing equation then reduces to

$$\frac{\partial \Delta T(z,t)}{\partial t} = \kappa \frac{\partial^2 \Delta T(z,t)}{\partial z^2} \tag{3.15a}$$

with the boundary conditions

$$\Delta T(z,t) = 0 \quad \text{for} \quad t \leqslant 0, \tag{3.15b}$$

$$\Delta T(z,t) \to 0 \quad \text{as} \quad z \to -\infty, \tag{3.15c}$$

$$\kappa\rho C_p \frac{\partial \Delta T(z,t)}{\partial z} = -Q(t) \quad \text{at} \quad z = 0, \tag{3.15d}$$

where Q is the upward heat flux, κ is the thermal diffusivity of water, ρ the density of water, and C_p the specific heat (at constant pressure) of water. As for the surface velocity, the temperature profile in the water is given by

$$\Delta T(z,t) = \sum_k \alpha_k \Gamma(k+1) \frac{-1}{\sqrt{\kappa}\rho C_p} \frac{2^{k+1}}{\sqrt{\pi}} t^{(k+1/2)} \exp(-z^2/8\kappa t) D_{-2(k+1)} \left(\sqrt{\frac{z^2}{8\kappa t}} \right), \tag{3.16}$$

provided that the heat flux is described as a power series in time:

$$Q(t) = \sum_k \alpha_k t^k. \tag{3.17}$$

The temperature deviation at the surface ΔT_o is then given by

$$\Delta T_0(t) = \sum_k \alpha_k \frac{\Gamma(k+1)}{\Gamma(k+3/2)} \frac{-1}{\sqrt{\kappa}\rho C_p} t^{(k+1/2)} = -Q(t) \frac{\Gamma(k+1)}{\Gamma(k+3/2)} \frac{\sqrt{t}}{\sqrt{\kappa}\rho C_p}. \tag{3.18}$$

Now, we further assume that $Q(t)$ is dominated by the latent heat flux:

$$Q(t) = \rho_a L_e C_e (q_s - q) U_a(t), \tag{3.19}$$

where L_e is the latent heat of evaporation, $U_a(t)$ the wind speed, q the specific humidity and q_s the specific humidity at saturation, ρ_a the density of moist air, and C_e an arbitrary constant also referred to as the Dalton number.

Figure 18 shows the data of figure 17(b) along with the prediction of equation (3.18) where the time-dependent surface heat flux is calculated by fitting an order-ten polynomial to the wind speed (figure 2) and using $C_e = 3.5 \times 10^{-3}$. As for the surface velocity, the long-time behaviour exhibits a $t^{1/2}$ time dependence, indicating that the heat flux has reached a constant value.

3.10. *Scaling the instabilities: waves and Langmuir circulations*

The results summarized in figure 11 do not directly compare well with those of Melville *et al.* (1998) who conducted experiments in the same facility before it was fitted with an improved wind-tunnel section and inlet. For example, at a final wind speed of $3\,\mathrm{m\,s^{-1}}$, they observed $\lambda_c = 7.5\,\mathrm{cm}$ while figure 11 shows $\lambda_c = 5.43\,\mathrm{cm}$ at the same final wind speed. Also, the inception times of the Langmuir circulations do not compare well. These differences are most likely due to the differences in the wind-tunnel and inlet sections following the modifications described in § 2. Yet, their successful scaling of the velocity profile in the water using the viscous diffusion scale, and the good agreement between our laminar model and the data lead us to expect that a common scaling should reconcile the data. Figure 19 shows the length scale of the cells, λ_c as a function of the shear layer depth at the time of the instability, for the data presented here and that of Melville *et al.* (1998). The data collapse onto a single curve suggesting that the scaling of the Langmuir circulations is controlled by the depth of the laminar shear layer. Up to the inception of the Langmuir circulations, the evolution of the surface velocity and temperature is monotonic (figure 10 and figure 13). It is therefore possible to calculate both the Reynolds and Rayleigh

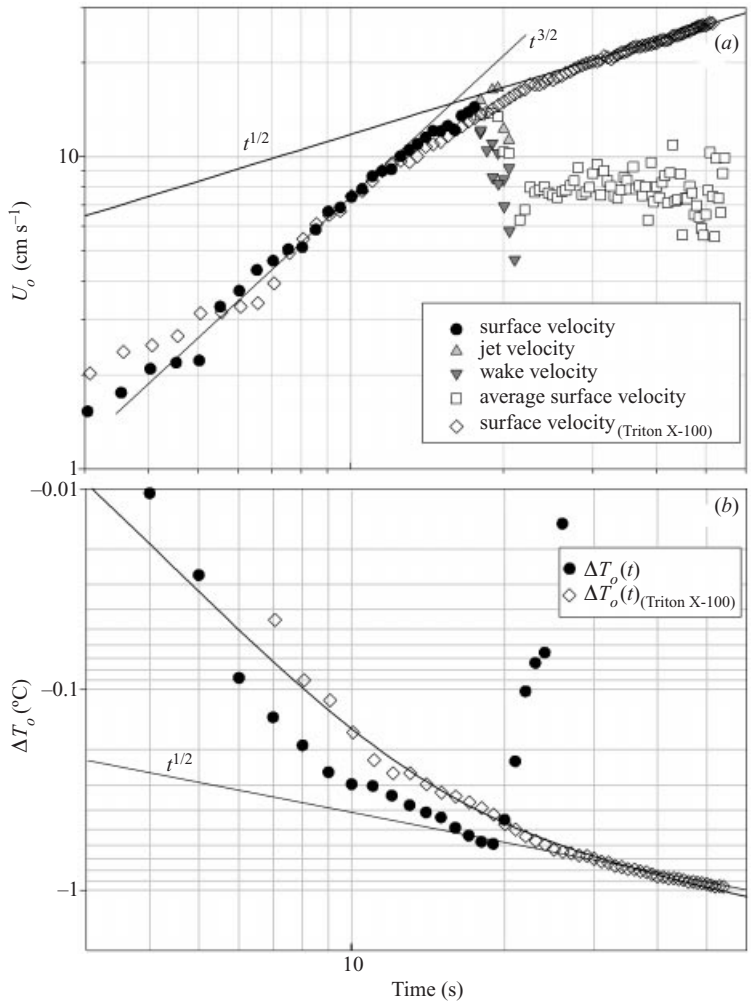

FIGURE 18. (*a*) Surface velocity for a final wind speed of $5\,\mathrm{m\,s^{-1}}$ and a fetch of 10.72 m with and without Triton X-100 added to the water (cf. figure 17*a*); the solid lines are the linear stress ($t^{3/2}$-dependence) and the constant stress ($t^{1/2}$-dependence) relations. (*b*) The data of figure 17(*b*) and the prediction from equation (3.18) where the surface heat flux $Q(t)$ is based on the wind speed according to equation (3.19). Also shown is the constant heat flux ($t^{1/2}$-dependence).

numbers based on the surface parameters:

$$Re = \frac{U_0\sqrt{\nu t}}{\nu} \tag{3.20}$$

and

$$Ra = \frac{\alpha(T_0 - T_B)g(\kappa t)^{3/2}}{\kappa\nu} = \frac{\alpha\Delta T_0 g(\kappa t)^{3/2}}{\kappa\nu} \tag{3.21}$$

respectively, where α is the thermal expansion coefficient, and T_B the bulk temperature. Figure 20 shows the relation between Rayleigh and Reynolds numbers prior to the observation of Langmuir cells. First, it appears that the Rayleigh number, for all wind speeds, is subcritical compared to the usual values for thermal instability (e.g. Ra_c, the critical Rayleigh number for free–free surface boundary conditions is approximately

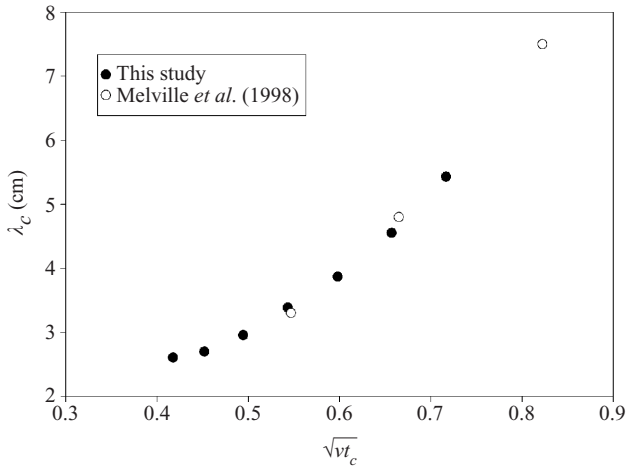

FIGURE 19. Wavelength of the Langmuir circulation λ_c as a function of the depth of the shear layer at the inception time t_c.

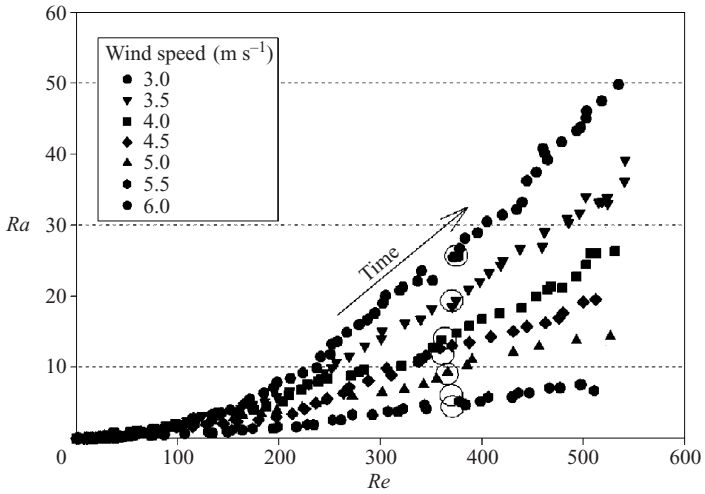

FIGURE 20. Rayleigh number versus Reynolds number up to the inception of the Langmuir circulations. The symbols show the different wind speeds. Length scales are based on the molecular diffusion of heat and momentum. The open circles mark the onset of the measurable surface waves.

$Ra_c = 650$; Drazin & Reid 1981). This indicates that the instability described here is almost certainly not thermally driven. Moreover, figure 20 shows that the Langmuir circulations arise at a Reynolds number of approximately 530 over the range of experimental conditions, independent of the wind speed. This suggests that Langmuir circulations are mechanically, not thermally driven, although evaporative cooling may contribute to the instability. The open circles in figure 20 show that the first detectable waves also appear at a relatively constant Reynolds number.

3.11. *Heat and gas transfer*

It is now evident that the instability of the surface shear flow to Langmuir circulations, and the subsequent rapid transition to turbulence, may be an important transition in the transfer of momentum, heat and gas across the surface of natural water bodies at

low wind speeds. Gas transfer in particular is controlled by the smaller scales (Jähne & Haußecker 1998) in the water. Current understanding and gas transfer models rely on so-called surface renewal models which assume that random turbulent motions break the cool, viscous surface layer thereby bringing unsaturated water parcels in contact with the air. Some models also take into account the increased surface area between the two phases due to capillary waves and entrained bubbles. Recently, Zappa (1999) has shown that micro-breaking (the breaking of gravity–capillary waves without significant air entrainment) breaks the skin layer and greatly contributes to the total gas transfer. However, as opposed to micro-beakers, which renew only a fraction of the surface layer, the instability reported here rapidly renews the whole surface.

One method for the proxy measurement of gas transfer across the water surface is the controlled flux technique (CFT) where a known heat flux is imposed across the surface and related to gas fluxes via a Schmidt number (Sc) relationship. Jähne *et al.* (1989) first suggested using this technique to infer the transfer velocity of gases across the surface.† It was further developed by Haußecker, Reinelt & Jähne *et al.* (1995) who used a CO_2 laser to heat the surface of the water locally. They showed that the decay of the heat spot could then be used to calculate the time constant t_* related to the heat transfer velocity, k_h, across the surface by

$$k_h = \sqrt{\kappa/t_*}, \tag{3.22}$$

with the gas transfer velocity k_g given by

$$k_g = k_h(Sc_h/Sc_g)^n, \tag{3.23}$$

where n is a parameter between $1/2$ and $2/3$ and Sc_h and Sc_g are the Schmidt numbers for heat and gas, respectively. The time constant t_* is the e-folding time of the heat spot laid down on the surface (figure 4). It follows that rapid decay of the spot corresponds to a high transfer velocity (equation (3.22)). Looking at figure 4, one can see that the heat marker laid down by the CO_2 laser persists for 1.5 to 2 s prior to the inception of the Langmuir circulations ($t = 18.3$ s) but disappears in approximately $1/2$ s when the flow has transitioned to being fully turbulent ($t > 22.8$ s). This implies that the heat and gas transfer velocities are increased by a factor of 1.7 to 2 by the Langmuir circulations.

Figure 21 shows a summary of the time series for the streamwise velocity at the surface, the surface temperature, the wave slope variance, and the inferred gas transfer velocity normalized to a Schmidt number of 600 (that of CO_2). The data shown are taken for a final wind speed of $5\,\mathrm{m\,s^{-1}}$ and a fetch of 10.72 m. It is clear that Langmuir circulations provide a very efficient mechanism for disrupting the momentum and thermal surface boundary layers. The gas transfer rates are also affected by the transition to Langmuir circulations. For the case presented here, a 70% increase in gas transfer velocity is observed to be directly correlated with the inception of the Langmuir circulations and the subsequent turbulence.

4. Field observations

We have seen in the laboratory that small-scale Langmuir circulations are an important mechanism for the transport of momentum and heat from the surface to

† This technique appears to be appropriate in the absence of air entrainment but bubble-mediated gas transfer at higher wind speeds has no counterpart in surface heat transfer (Melville 1996).

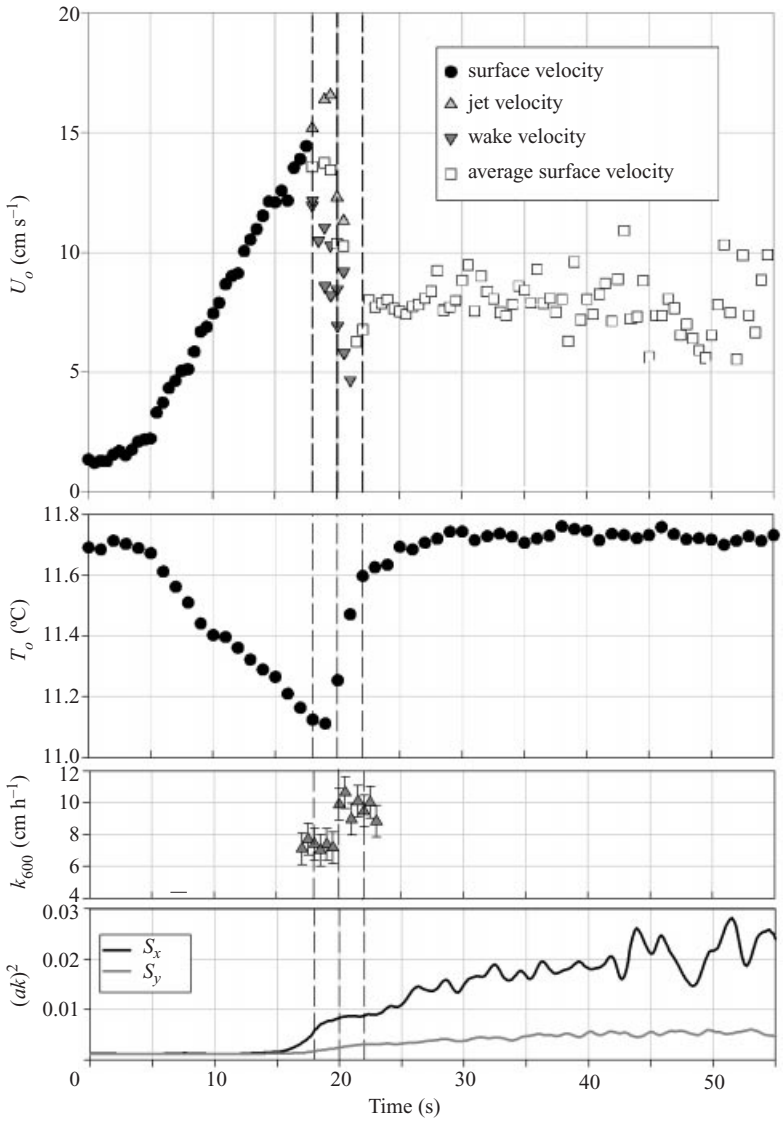

FIGURE 21. Summary time series for the surface velocity, temperature, gas transfer velocity normalized to a Schmidt number of 600, and surface slope variance. The data shown are taken for a final wind speed of 5 m s^{-1} and a fetch of 10.72 m.

depth. They also appear to very rapidly renew a large fraction of the surface skin layer. If present in the field, these small-scale circulations may have important implications for the fluxes of gas, heat and momentum between the ocean and the atmosphere. Field observations of Langmuir circulations generally report on the larger scales that are measured by the Doppler sonars which typically have resolutions on the order of a metre or more. However, we have shown that the phenomena observed in the laboratory are of smaller scales. The available field observations report on flows where the Langmuir circulations are superimposed on turbulence and can be isolated by coherent averaging or filtering. Due to their small scale and short persistence times, existing field observations of centimetre-scale Langmuir circulations are usually

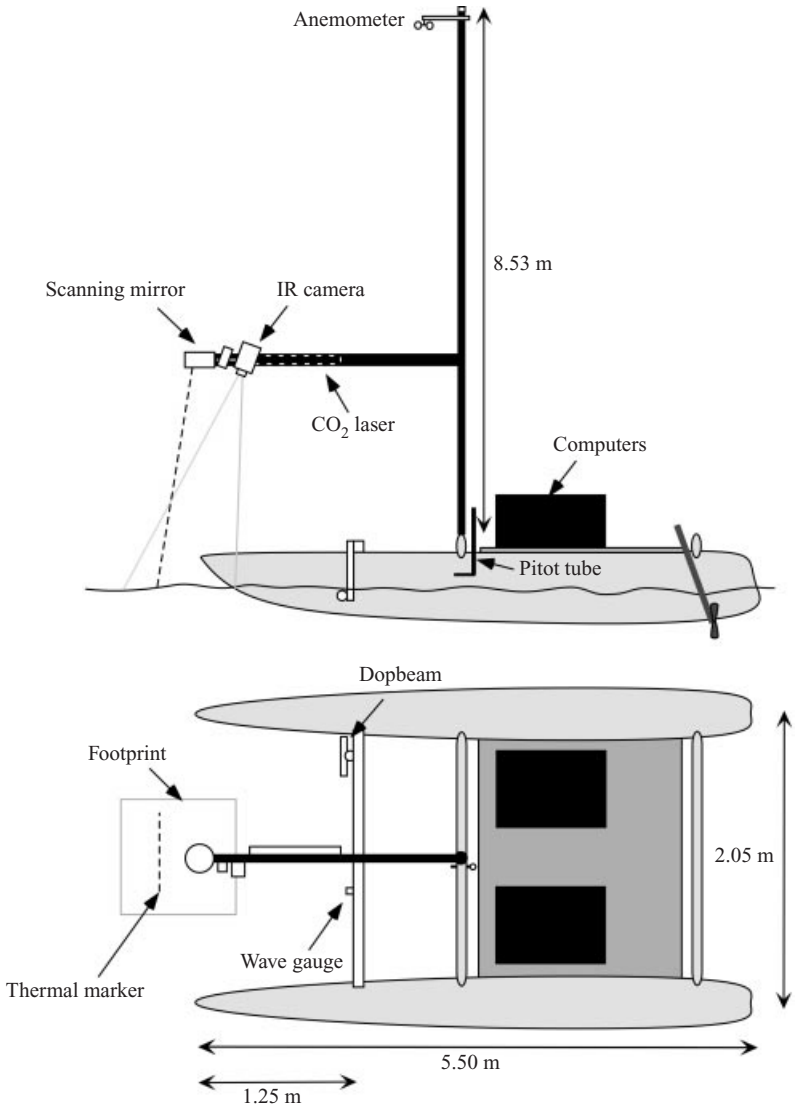

FIGURE 22. Instrumentation setup on the catamaran.

qualitative and based on photographic data (Owen 1966; Scott *et al.* 1969; Kenney 1993; Szeri 1996). This section reports on a short experiment designed to observe, in the field, the phenomena that were studied in the laboratory and described in the preceding sections.

Most unambiguous field observations of small-scale Langmuir circulations have been made in lakes or lagoons. At sea, the presence of large gravity waves and breaking waves disrupt the gravity–capillary wave field (Melville, Veron & White 2001) and greatly deform the surface which makes it more difficult for an observer to notice the streaky small-scale structures (figure 15, p. 35). Therefore, it was decided to perform the experiment in a small water body and we selected the model yacht basin

in Mission Bay, San Diego, which has previously been used for wind-wave studies (Van Dorn 1953). The basin is a 240 m by 60 m pond roughly aligned in the east–west direction. It has a constant water depth of approximately 2.5 m and gently sloping sides. It is filled with salt-water from Mission Bay.

4.1. *Instrumentation*

A commercial 18 ft (5.5 m) catamaran (Hobie Cat) was specially modified for the experiment. The compliant trampoline was replaced with a hardwood deck and fitted with two large splash-proof housings for computer and electronic equipment. The mast was reversed (back to front) so that the boom would be pointing towards the bow and could be used to support instrumentation at the desired height above the water level. The IR camera, the CO_2 laser, the scanning mirror, and the colour camera were placed on the boom in order to reach as far as possible beyond the bows. Temperature, humidity and wind speed sensors were placed at the top of the mast (9 m). A resistance-wire wave gauge, a Pitot-static tube in the air, and a coherent acoustic-Doppler profiling current meter (Dopbeam, Sontek, San Diego) were placed between the two hulls. The Dopbeam was oriented with its acoustic beam perpendicular to the hulls, parallel to the water surface at a depth of approximately 5 to 8 cm. All the equipment, with the exception of the Dopbeam, is the same as that described in § 2. The Dopbeam and its use is described in detail in Veron & Melville (1999*b*). It is a coherent Doppler sonar with $O(1)$ m, range and an $O(1)$ cm resolution, which permits the direct measurement of the wavenumber spectrum of the turbulence (in the inertial subrange), and hence the dissipation of turbulent kinetic energy (TKE). It was set to operate with a 625 Hz ping rate. Averaging of consecutive profiles reduced the final data rate to 25 Hz. A total of 2 min of data was acquired for each data file. Figure 22 shows a diagram of the equipment setup and the instrumented catamaran. All instruments on the catamaran were synchronized and powered from shore with a small gasoline generator and a water-resistant power cable suspended at the surface by floats.

4.2. *Results*

The experiment was performed from sunrise to approximately 10–11 a.m. in order to observe, as in the laboratory, the transition from a quiescent to a fully turbulent, wavy surface, as the wind increased. The catamaran was oriented in the east–west direction, facing into the wind (from the west), at a fetch of approximately 200 m. Data were taken on 29 and 31 March and 4, 6 and 7 April 2000.

4.2.1. *Environmental data*

The wave height and wind speed were sampled using the same equipment and sampling rate as in the laboratory (200 Hz). During the course of the experiment (from sunrise to 11 am), the wind rose from nearly zero to typically 5–6 m s^{-1}. During that time, surface waves were generated, grew and eventually became fetch-limited. The surface flow also evolved from quiescent to turbulent. Figure 23 shows an example of the wind speed recorded by the mast anemometer, U_9, and the Pitot-static tube at 20 cm above the water surface, $U_{0.2}$ on 4 April 2000. In approximately 3 hours, the average wind speed U_9 rose from 2 to 6 m s^{-1}, where $U_{0.2}$ and U_9 are averaged over 75 s and 150 s, respectively. Figure 23 also shows the variance of the wave field recorded by the wave gauge. The variance is obtained by integration of the surface wave frequency spectra from 1 Hz to 30 Hz. Each spectrum is calculated for 75 s using

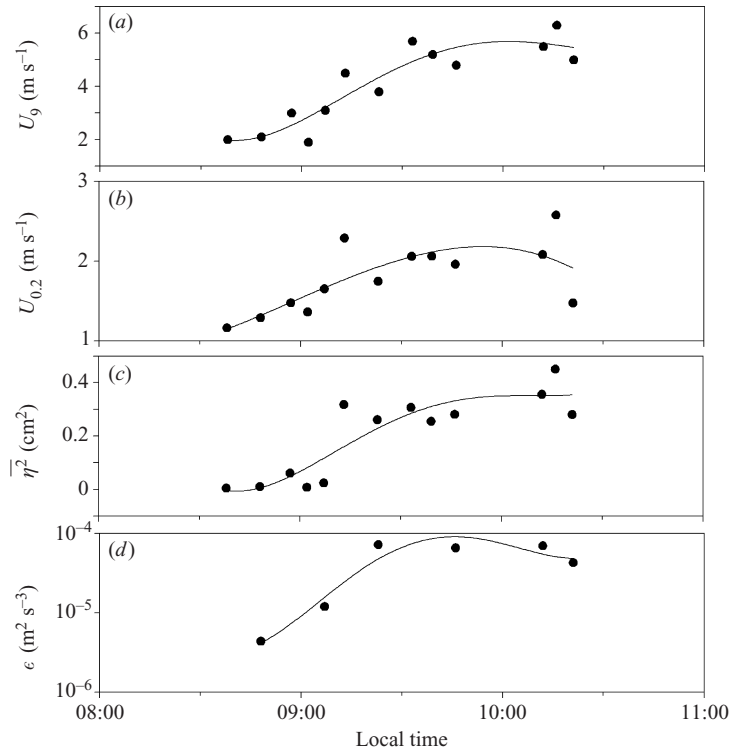

FIGURE 23. (*a*) Wind speed at 9 m above the water surface (150 s average), (*b*) wind speed at 20 cm above the water surface (75 s) average, (*c*) wave height variance (75 s average), (*d*) turbulent kinetic energy dissipation.

1 s windows with 50% overlap. As expected, with time, the power spectral density of the wave field grows and the peak frequency shifts from approximately 5 to 2.2 Hz.

4.2.2. *Surface flow visualization*

The transition between the quiescent and the turbulent surface-flow states occurs in patches when localized increases in the wind speed first ripple the surface. These local patches advecting with the wind, or 'cat's paws', are areas of the surface in which gravity–capillary waves are generated, and where the surface accelerates under the effect of the wind stress. These conditions are similar to those of the laboratory experiments and the data taken with the IR camera confirm that, within the cat's paws, the surface undergoes a transition similar to that found in the laboratory. Figure 24 shows a series of surface temperature images taken with the IR camera on 4 April 2000. The images are separated by 1 s and the image size is 53.35 cm $\times$ 53.35 cm. As for the transition observed in the laboratory, the surface flow exhibits the development of longitudinal wakes associated with regions of local upwelling of warmer fluid from the bulk fluid below. The colder surface jets also become unstable, driving the surface flow into a fully turbulent state. The average surface temperature increases during the time period shown as the surface is rapidly renewed. Figure 24 also shows the wind speed recorded by the Pitot-static tube and the wave gauge record during the event. The triangles denote the times at which the surface temperature are shown. The instabilities appear to be associated with a local and rapid increase in the wind speed. Note that the wave height also increases during this time period, presumably

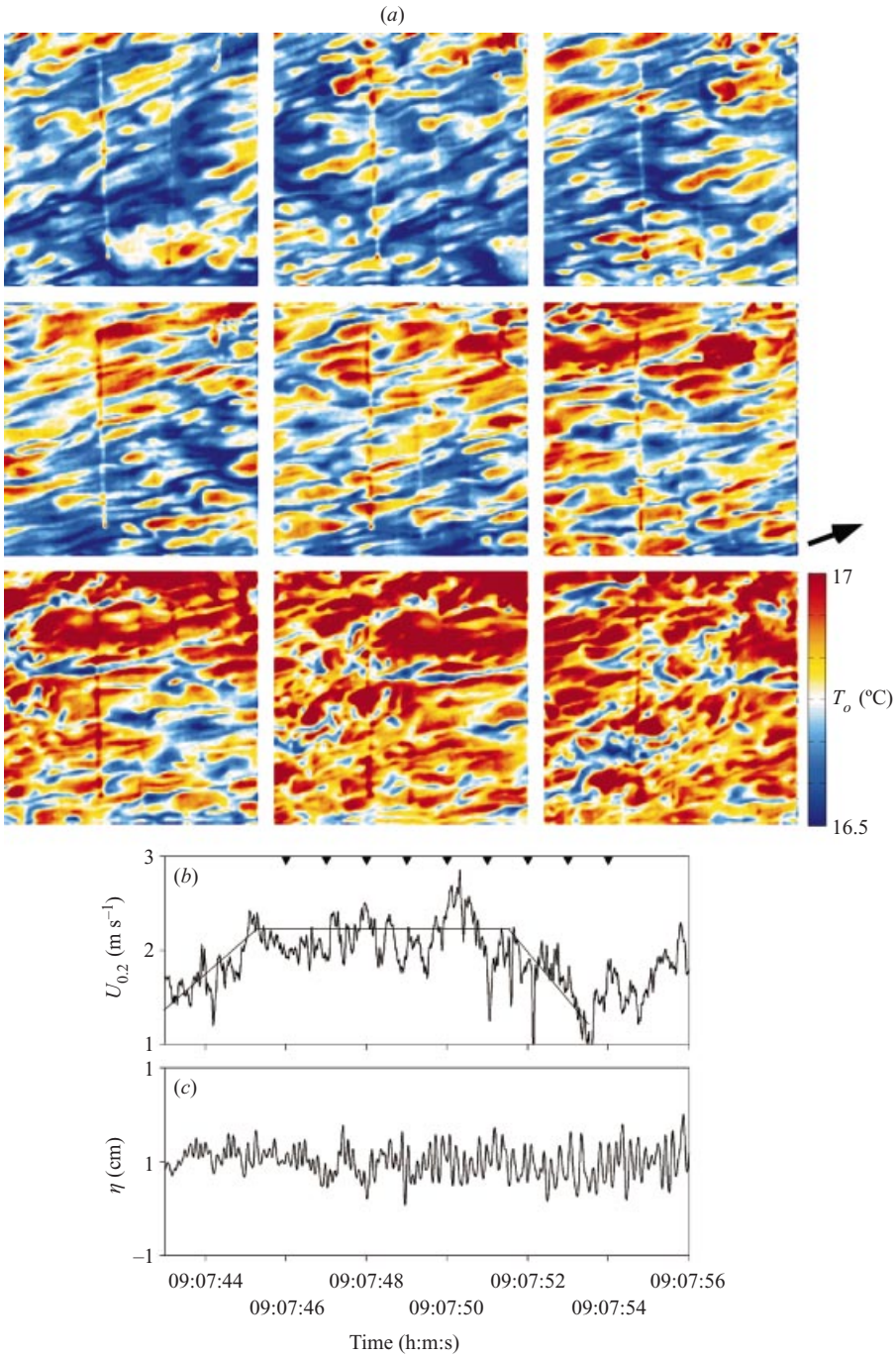

FIGURE 24. (*a*) Surface temperature images taken on 4 April 2000. Image size is 53.35 cm × 53.35 cm. Times shown are t = 09:07:46 to 09:07:54 a.m. at 1 s intervals (left to right, top to botton). The wind direction is given by the arrow. Note the evolution of the surface temperature as the surface is disrupted by the Langmuir circulations. Note also that the average surface temperature increases. (*b*) Time series of the wind speed and (*c*) wave heights. Note the variability in the wind speed and the growth of the wave amplitude. The inverted triangles denote the times of the IR images shown in (*a*).

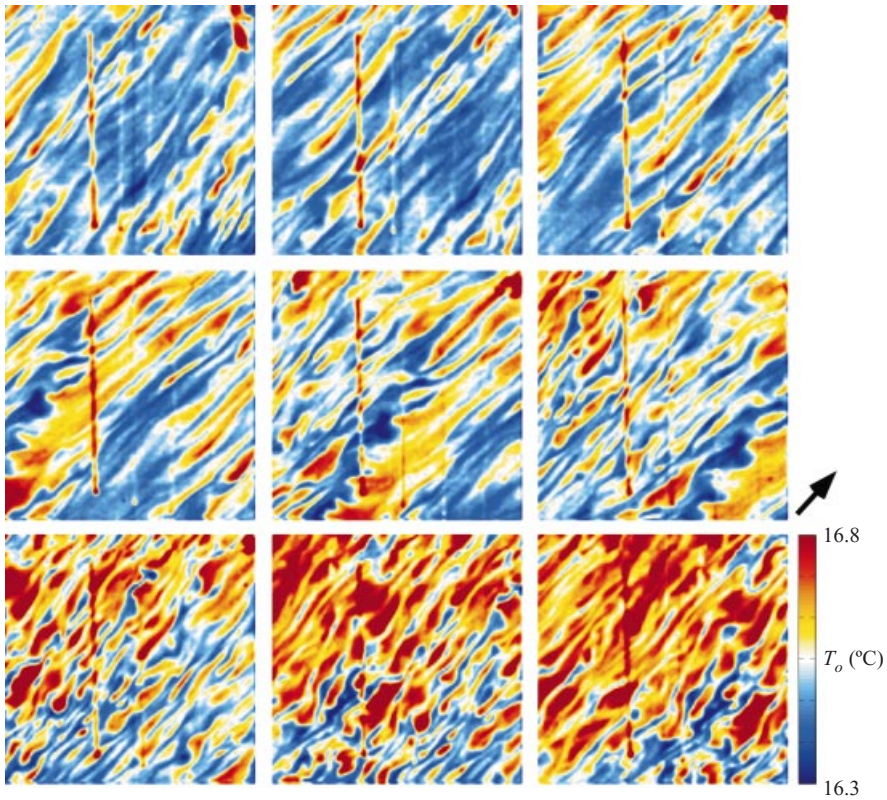

FIGURE 25. Surface temperature field for $t = 09{:}07{:}11$ to $09{:}07{:}19$ a.m. on 4 April 2000. Images are shown 1 s and the image size is 53.35 cm × 53.35 cm. The wind direction is given by the arrow.

under the influence of the wind. Spectral analysis of the infrared images shows that the structures have a cross-wind wavelength of approximately 3.5–4 cm while the wind speed at 9 m height was rising from 3.1 to 4.5 m s^{-1}. These values compare well with the laboratory data (see figure 11), especially considering the large and rapid variability in the near-surface wind speed (figure 24*b*)

These events are local and transient, as is the wind. Visual observation reveals that once the wind speed decreases, the waves rapidly propagate away and the surface re-establishes its glassy appearance. The IR images confirm that the surface skin layer is re-established rapidly after the wind decreases significantly. Yet, if another rapid increase in the wind speed occurs, the surface flow will again develop Langmuir circulations that will rapidly disrupt the surface momentum and thermal boundary layers. Figure 25 shows a series of surface temperature images taken with the IR camera on 4 April, only 30 s before the data shown in figure 24. Once again, the surface flow shows the development of organized longitudinal warmer structures where the water is upwelling. The Langmuir circulations are quickly followed by a transition to fully turbulent flow. As for the data of figure 24, the average surface temperature is increased by approximately 0.5 °C and the cross-wind length scale is approximately 3.8 cm.

4.2.3. *Sub-surface turbulence*

The sub-surface velocity field was measured with the Dopbeam. The spatial velocity profile measured by the sonar permits a direct calculation of the velocity

wavenumber spectrum $\Phi(k)$. When an inertial subrange in the turbulence is present, the wavenumber spectrum of the velocity can be expressed as

$$\Phi(k) = Ak^{-5/3}\epsilon^{2/3}, \tag{4.1}$$

where ϵ is the TKE dissipation. During the experiments, we observed an increase in sub-surface turbulence levels. For example, on 4 April, the spectral levels increase by a factor of approximately 5 with time and appear to stabilize after 9:13 a.m., the time at which the surface flow is fully turbulent and quasi-steady. This increase corresponds to more than an order of magnitude increase in the kinetic energy dissipation levels (figure 23). Since the velocity recorded by the Dopbeam is aligned with the cross-wind direction and is therefore minimally affected by the orbital motion of the surface waves, and since the surface wave field and the IR images at 9:13 a.m. did not show evidence of micro-scale wave breaking, the elevation in the kinetic energy dissipation is attributed to the cross-wind velocity and the turbulence induced by the Langmuir circulations within the cat's paws such as those shown in figures 24 and 25.

5. Discussion

5.1. *Field observations*

The field data show that the transitional phenomena seen in the laboratory (wave generation and Langmuir circulations) are also seen in the field under similar wind conditions. The Doppler sonar measurements showed that, during the experiment, the transition between the quiescent (at sunrise) and the fully turbulent surface flow (10–11 a.m.) correlated with a significant increase in the TKE dissipation levels. This can be seen in figure 23 where the TKE begins to increase between 09:07 and 09:23, the time at which the first signs of the surface transition appeared within surface cat's paws (figure 24 and figure 25). We anticipate that, in the absence of surface wave breaking, these small-scale Langmuir circulations are likely to be the dominant source of turbulence at the surface, and thus a controlling factor in ocean–atmosphere exchanges, at low wind speed ($< 6\,\mathrm{m\,s^{-1}}$).

In the field, we have observed that the evolution of the surface flow is local and intermittent, and is followed by a rapid re-establishment of stable surface flow conditions once the wind has died. This quick evolution from laminar flow to turbulence through the development and evolution of surface waves and small-scale Langmuir circulations, and back to laminar, allowed multiple occurrences of these instabilities. This has important implications for upper ocean processes. In the field, the wind is typically gusty and therefore intermittently generates waves. These data suggest that the local generation of the waves will be accompanied by a swift surface renewal and injection of vorticity caused by the associated Langmuir circulations.

5.2. *Sea-surface temperature and the surface skin layer*

The very top layer of the ocean surface, referred to as the skin layer, is typically a few tenths of degree colder than the bulk of the water just below. It is this small temperature difference which permitted the visualization of the Langmuir circulations by IR imaging in the work presented here. However, the bulk–skin temperature difference ΔT, has recently received considerable attention because of its importance for air–sea heat transfer and for biases in remote sea-surface temperature measurements, especially when the heat capacity of the water is so much greater than that of the (dry) atmosphere. In the experiments reported her, both in the laboratory and the field, it is the Langmuir circulations and not wave breaking that first destroy

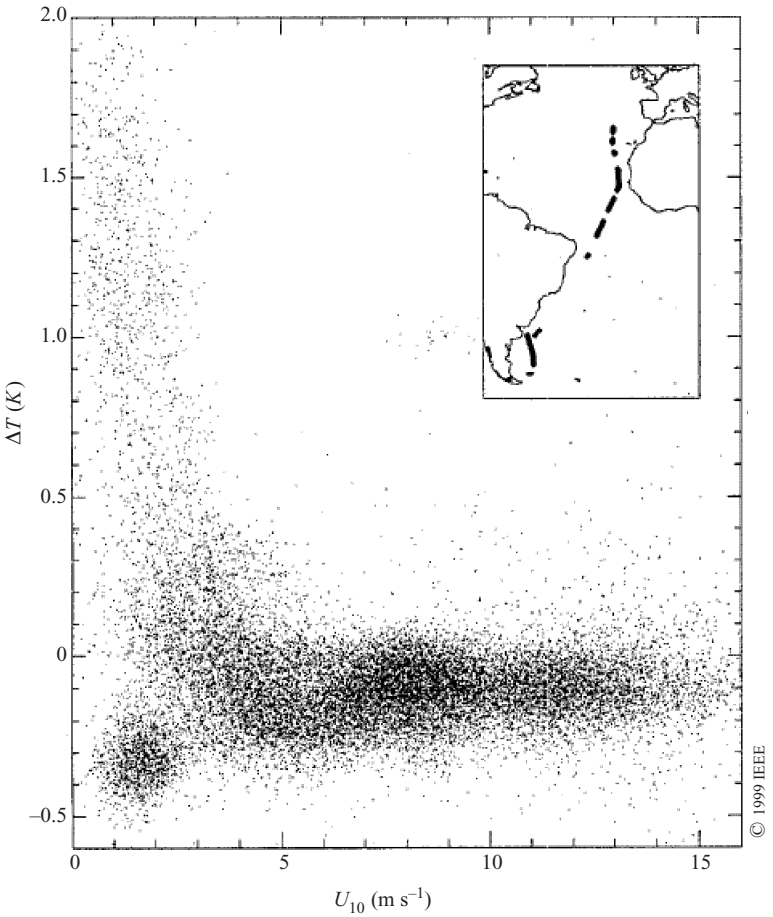

FIGURE 26. 10 m wind speed plotted against ΔT for the entire Atlantic AMT-3 data set (from Donlon *et al.* 1999).

the cool surface skin, although if the winds are sustained microscale breaking may quickly follow. Nevertheless, it is possible that the phenomenon described here is a controlling factor of the temperature amplitude of the cool skin at low wind speeds. For example, figure 26 shows measurements by Donlon, Eifler & Nightingale (1999) of ΔT as a function of wind speed for data spanning the North and South Atlantic. It is clear from their figure that the variance in the bulk–skin temperature difference is dramatically reduced for wind speeds above 3 to 4 m s^{-1}. Donlon *et al.* (1999) suggested that as the wind speed decreases, the role of shear turbulent heat transfer gradually diminishes, so that molecular and convective heat transfer dominate.

However, the data do not show a gradual, but rather a sharp change indicating at least two distinct regimes. Since our laboratory and field data show that a minimum wind speed of about 2–3 m s^{-1} is necessary for the Langmuir circulations to occur, we suggest that small-scale Langmuir circulations may play a role in determining ΔT at these transitional wind speeds. The large scatter in the data below 3 m s^{-1} is the sign that ΔT is influenced by a range of processes that are probably intermittent in space and time, whereas the small variability above 3 m s^{-1} is consistent with our observations of transition to turbulence generated by the Langmuir circulations, and subsequently breaking.

5.3. *Air–sea gas transfer*

With the increase of anthropogenic 'green-house gases' released into the atmosphere since the industrial revolution in the late 18th century, the study of gas transfer between the oceans and the atmosphere has become of paramount importance. The ocean is a large reservoir of carbon and is believed to absorb, across its surface, approximately half the carbon of anthropogenic origin (Etcheto & Merlivat 1988). Historically, gas transfer rates, based on laboratory data, were parameterized as a function of the wind speed. Liss & Merlivat (1986) proposed a piecewise linear parameterization with a first transition at a wind speed of $3.6\,\mathrm{m\,s^{-1}}$ corresponding to the transition between what was called the smooth and the rough surface regions. This transition was based on several studies that reported a sudden increase in gas transfer rates when waves first appeared. Specifically, Broecker, Petermann & Siems (1978) reported that the gas flux was strongly enhanced with the formation of capillary waves at approximately $2\,\mathrm{m\,s^{-1}}$ wind speed. This increase was first attributed to the increased surface area due to the waves. Subsequently, Liss (1983) suggested that

> ...capillary waves themselves may not be the cause of the observed enhancement, but merely act as indicators of a change in the nature of gas transfer process in water close to the air-water interface.

Later, Hasse (1990) confirmed that including the waves in the gas transfer processes did not explain the magnitude of the enhancement. Jähne *et al.* (1987) found that the Schmidt number dependence of the gas transfer velocity changed with the onset of the waves, indicating a different surface boundary condition. Finally, Tang & Wu (1992) suggested that the sudden increase in gas transfer when waves first appear is associated with the transition of the water boundary layer from viscous to turbulent.

The present work suggests that the onset of the waves, as far as gas transfer is concerned, is simply a sign of the almost simultaneous formation of the Langmuir circulations and the accompanying transition of the surface flow from laminar to turbulent. In fact, figure 21 shows a sudden increase in gas transfer velocity with the formation of the Langmuir circulations rather than the surface waves. However, the fact that both phenomena are strongly coupled, exacerbated by the fact that the Langmuir circulation transition has eluded observation, have likely led to the correlation of the abrupt increase in the gas transfer velocity with the onset of the waves.

6. Conclusions

We have shown that for a wind-driven water surface starting from rest, both the surface velocity and temperature evolve monotonically up to the inception of the Langmuir circulations which arise as an instability of the laminar wavy shear flow. This instability provides a very efficient mechanism for disrupting the momentum and thermal surface boundary layers. Heat and vorticity are then mixed into the bulk of the fluid at rates greater than those associated with molecular diffusion. The heat (and gas) transfer rates too are affected by this transition. In fact, we have observed a sudden increase in heat transfer velocity that is coincident with the inception of the Langmuir circulations and the subsequent turbulence rather than the inception of surface waves.

Using active imaging techniques, we have measured the velocity of the surface of the water in both the laminar and turbulent regimes, and shown that within the range of the experiments, the Langmuir circulations appear at a constant Reynolds number of 530 ± 20 (based on the surface velocity and the shear layer depth) indicating that the

mechanism for the instability is mechanical rather than thermal. The Reynolds number scaling is supported by theoretical predictions of the development of the laminar shear layer under different surface stress regimes.We conclude that the observed instability leads to the transition from a laminar to turbulent wind-driven surface shear flow. Importantly, it is the Langmuir circulations and not wave breaking that first destroy the cool surface skin. It is possible that the phenomenon described here is a controlling factor of the temperature of the cool skin of the ocean surface at low wind speeds.

Within the range and accuracy of these experiments, we have shown that surface waves are first observed at a Reynolds number of 370 ± 10, preceding the instability to Langmuir circulations. Furthermore, we observed that the length and time scales associated with the generation of the surface waves and the Langmuir circulations are comparable. In the context of the CLII mechanisms, the problem studied here is clearly of order unity where the surface velocity is comparable to the surface-wave phase speed. This leads to a clear coupling of the Langmuir cells with the surface waves and the subsequent cross-wind (three-dimensional) modulation of the wave field. These observations imply that even the early stages of wind-wave evolution cannot be completely understood without the inclusion of the Langmuir circulations or wave–current interactions.

A short series of observations in the field under natural wind conditions has shown that Langmuir circulations are present in the field at similar time and length scales, under similar wind conditions. We observed that, under the influence of an increasing wind, the surface rapidly becomes unstable to surface wave modes and shortly thereafter to Langmuir circulations. The rapid evolution of the surface flow is local and intermittent, and is followed by a re-establishment of stable surface flow conditions when the wind subsides. This quick evolution from laminar to turbulent through the development and evolution of the small-scale Langmuir circulations, and back to laminar, permits several transitions to occur in only a few minutes. Therefore, a large fraction of the surface skin is rapidly renewed leading to enhanced mass, momentum and heat transfer. As in the laboratory, it is the Langmuir circulations, and not breaking surface waves, that first destroy the cool surface skin. The length and time scales associated with the generation of the surface waves and the Langmuir circulations in the field are also comparable to those in the laboratory. Visual observation in the field confirmed that the surface-wave field is modulated by the flow associated with the underlying Langmuir circulations.

Small-scale Langmuir circulations lead to significant sub-surface turbulence levels and therefore contribute significantly to the total kinetic energy dissipation. In the absence of surface wave breaking, at low wind speed, these small-scale Langmuir circulations are likely to be the dominant source of turbulence at the surface, and thus a controlling factor in air–sea fluxes at low wind speed.

We thank our colleagues at the Hydraulics Laboratory, Charles Coughran, Dave Aglietti and John Lyons. We are grateful to Jochen Klinke for providing the calibration for the colour imaging slope gauge. We thank two anonymous reviewers for comments that have improved the final version of the paper. This work was supported by NSF grants OCE 9633794 and OCE 9812182.

REFERENCES

Belcher, S. E. & Hunt, J. C. R. 1998 Turbulent flow over hills and waves. *Annu. Rev. Fluid Mech.* **30**, 507–538.

Broecker, H. C., Petermann, J. & Siems, W. 1978 The influence of wind on CO_2 exchange in a wind wave tunnel, including the effect of monolayers. *J. Mar. Res.* **36**, 595–610.

Caulliez, G., Ricci, N. & Dupont, R. 1998 The generation of the first visible wind waves. *Phys. Fluids* **10**, 757–759.

Cox, C. S. 1958 Measurement of slope of high frequency waves. *J. Mar. Res.* **16**, 199–225.

Craik, A. D. D. 1977 The generation of Langmuir circulations by an instability mechanism. *J. Fluid Mech.* **81**, 209–223.

Craik, A. D. D. 1982*a* The generalized Lagrangian-mean equations and hydrodynamic stability. *J. Fluid Mech.* **125**, 27–35.

Craik, A. D. D. 1982*b* Wave-induced longitudinal-vortex instability in shear flows. *J. Fluid Mech.* **125**, 37–52.

Donlon, C. J., Eifler, W. & Nightindale, T. J. 1999 The thermal skin temperature of the ocean at high wind speed. *Proc. IGARSS Conf. Hamburg, Germany*.

Downing, H. D. & Williams, D. 1975 Optical constant of water in the infrared. *J. Geophys. Res.* **80**, 1656–1661.

Drazin. P. G. & Reid, W. H. 1981 *Hydrodynamic Stability*. Cambridge University Press.

Ebuchi, N., Kawamura, H. & Toba, Y. 1987 Fine structure of laboratory wind-wave surfaces studied using optical method. *Boundary-Layer Met.* **39**, 133–151.

Etcheto, J. & Merlivat, L. 1988 Satellite determination of the carbon dioxide exchange coefficient at the ocean atmosphere interface: a first step. *J. Geophys. Res.* **93**, 15669–15678.

Fedorov, A. V. & Melville, W. K. 1998 Nonlinear gravity-capillary waves with forcing and dissipation. *J. Fluid Mech.* **354**, 1–42.

Hasse, L. 1990 On the mechanism of gas exchange at the air-sea interface. *Tellus* **42B**, 250–253

Haußecker, H. 1996 Messung und simulation von kleinskaligen austauschvorgangen an de ozeanoberflache mittels thermographie. Dissertation, Universitat Heidelberg.

Haußecker, H., Reinelt, S. & Jähne, B. 1995 Heat as a proxy tracer for gas exchange measurements in the field: Principles and technical realization. *Third Int. Symp. on Air Water Gas Transfer* (ed. B. Jahne & E. C. Monahan).

Henderson, D. M. 1998 Effects of surfactants on Faraday-wave dynamics. *J. Fluid Mech.* **356**, 89–107.

Jähne, B. & Haußecker, H. 1998 Air water gas exchange. *Annu. Rev. Fluid Mech.* **30**, 443–468.

Jähne, B., Libner, P., Fischer, R., Billen, T. & Plate, E. J. 1989 Investigating the transfer processes across the free aqueous viscous boundary layer by the controlled flux method. *Tellus* **41B**, 177–195.

Jähne, B., Munnich, K. O., Bosinger, R., Dutzi, A., Huber, W. & Libner, W. 1987 On the parameters influencing air-water gas exchange. *J. Geophys. Res.* **92**, 1937–1949.

Jähne, B. & Riemer, K. 1990 Two-dimensional wave number spectra of small-scale water surface waves. *J. Geophys. Res.* **95**, 11531–11546.

Jähne, B. & Wass, S. 1989 Optical measuring technique for small scale water surface waves. *Advanced Optical Instrumentation for Remote Sensing of the Earth's Surface, SPIE Con. Proc.* 1129, pp. 122–128.

Katsaros, K. B. 1980 The aqueous thermal boundary layer. *Boundary Layer Met.* **18**, 107–127.

Kawai, S. 1979 Generation of initial wavelets by instability of a coupled shear flow and their evolution to wind waves. *J. Fluid Mech.* **93**, 661–703.

Kenney, B. C. 1993 Observations of coherent bands of algae in a surface shear layer. *Limnol. Oceanogr.* **38**, 1059–1067.

Klinke, J. 1996 Optical measurements of small scale wind-generated water surface waves in the laboratory and the field. Dissertation, Universitat Heidelberg.

Langmuir, I. 1938 Surface motion of water induced by wind. *Science* **87**, 119–123.

Larson, T. R. & Wright, J. W. 1975 Wind-generated gravity capillary waves: laboratory measurements of temporal growth rates using microwave backscatter. *J. Fluid Mech.* **70**, 417–436.

Leibovich, S. 1977 On the evolution of the system of wind drift current and Langmuir circulations in the ocean. Part 1. Theory and average current. *J. Fluid Mech.* **79**, 715–743.

Leibovich, S. 1983 The form and dynamics of Langmuir circulations. *Annu. Rev. Fluid Mech.* **15**, 391–427.

Liss, L. 1983 Gas transfer: experiments and geochemical implications. *Air Sea Gas Exchanges and Particles* (ed. P. S. Liss & W. G. N. Slinn), pp. 241–298. Reidel.

Liss, P. S. & Merlivat, L. 1986 Air-sea gas exchange rates: introduction and synthesis. *The Role of Air-Sea Gas Exchange in Geochemical Cycling* (ed. P. Buat-Menard), pp. 113–129. Reidel.

Longuet-Higgins, M. S. 1995 Parasitic capillary waves: a direct calculation. *J. Fluid Mech.* **301**, 79–107.

Melville, W. K. 1996 The role of surface-wave breaking in air–sea interaction. *Annu. Rev. Fluid Mech.* **28**, 279–321.

Melville, W. K., Shear, R. & Veron, F. 1998 Laboratory measurements of the generation and evolution of Langmuir circulations. *J. Fluid Mech.* **364**, 31–58.

Melville, W. K., Veron, F. & White, C. J. 2001 The velocity field under breaking waves: coherent structures and turbulence. *J. Fluid Mech.* (in press).

Miles, J. W. 1957 On the generation of surface waves by shear flows. Part I. *J. Fluid Mech.* **3**, 185–204.

Owen, R. W. Jr. 1966 Small-scale, horizontal vortices in the surface layer of the sea. *J. Mar. Res.* **24**, 56–65.

Phillips, O. M. 1985 Spectral and statistical properties of the equilibrium range in wind-generated gravity waves. *J. Fluid Mech.* **156**, 505–531.

Phillips, W. R. C. & Wu, Z. 1994 On the instability of wave-catalysed longitudinal vortices in strong shear. *J. Fluid Mech.* **272**, 235–254.

Plueddemann, A. J., Smith, J. A., Farmer, D. M., Weller., R. A., Crawford, W. B., Pinkel, R., Vagle, S. & Gnanadesikan, A. 1996 Structure and variability of Langmuir circulation during the Surface Waves Process Program. *J. Geophys. Res.* **101**, 3525–3543.

Scott J. T., Meyer, G. E., Stewart, R. & Walther, E. G. 1969 On the mechanism of Langmuir circulations and their role in epilimnion mixing. *Limnol. Oceanogr.* **14**, 493–503.

Smith, J. A. 1992 Observed growth of Langmuir circulation. *J. Geophys. Res.* **97**, 5651–5664.

Smith, J. A. 1998 Evolution of Langmuir circulation during a storm. *J. Geophys. Res.* **103**, 12649–12668.

Smith, J. A., Pinkel, R. & Weller, R. A. 1987 Velocity fields in the mixed layer during MILDEX. *J. Phys. Oceanogr.* **22**, 350–360.

Szeri, A. J. 1996 Langmuir circulations in Rodeo Lagoon. *Mon. Weath. Rev.* **124**, 341–342.

Tang, S. & Wu, J. 1992 Suppression of wind-generated ripples by natural films, a laboratory study. *J. Geophys. Res.* **97**, 5301–5306.

Valenzuela, G. R. 1976 The growth of gravity-capillary waves in a coupled shear flow. *J. Fluid Mech.* **76**, 229–250.

Van Dorn, W. G. 1953 Wind stress in an artificial pond. *J. Mar. Res.* **12**, 249–276.

Veron, F. 2000 Turbulent mixing at the surface of natural water bodies: breaking waves and Langmuir circulations. PhD Thesis, University of California, San Diego.

Veron, F. & Melville, W. K. 1999*a* Pulse-to-pulse coherent Doppler measurements of waves and turbulence. *J. Atmos. Oceanic Tech.* **16**, 1580–1597.

Veron, F. & Melville, W. K. 1999*b* Laboratory studies of the initiation of Langmuir circulations and turbulence. *Fourth Intl Symp. on Air-Sea Interaction, Sydney, Australia* (ed. M. L. Banner), pp. 265–272.

Wheless, G. H. & Csanady, G. T. 1993 Instability waves on the air-sea interface. *J. Fluid Mech.* **248**, 363–381.

Zappa, C. J. 1999 Mircroscale wave breaking and its effect on air-water gas transfer using infrared imagery. PhD thesis, Applied Physics Laboratory, University of Washington, Seattle, Washington.

Zhang, X. 1995 Capillary-gravity waves generated in a wind wave tank: observations and theories. *J. Fluid Mech.* **289**, 51–82.

Zhang, X. & Cox, S. C. 1994 Measuring the two-dimensional structure of a wavy water surface optically: A surface gradient detector. *Exps. Fluids* **17**, 225–237.